





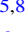







Code Comparison in Galaxy-scale Simulations with Resolved Supernova Feedback: Lagrangian versus Eulerian Methods

Chia-Yu Hu (胡家瑜)¹ , Matthew C. Smith^{2,3} , Romain Teyssier⁴ , Greg L. Bryan^{5,6} , Robbert Verbeke⁷, Andrew Emerick⁶ , Rachel S. Somerville⁵ , Blakesley Burkhart^{5,8} , Yuan Li (黎原)⁹ , John C. Forbes⁵ , and Tjitske Starkenburg¹⁰ 

¹ Max-Planck-Institut für Extraterrestrische Physik, Giessenbachstrasse 1, D-85748 Garching, Germany; cyhu.astro@gmail.com

² Universität Heidelberg, Zentrum für Astronomie, Institut für theoretische Astrophysik, Albert-Ueberle-Str. 2, D-69120 Heidelberg, Germany

³ Max-Planck-Institut für Astronomie, Königstuhl 17, D-69117 Heidelberg, Germany

⁴ Department of Astrophysical Sciences, Princeton University, Princeton, NJ 08544, USA

⁵ Center for Computational Astrophysics, Flatiron Institute, 162 5th Avenue, New York, NY 10010, USA

⁶ Department of Astronomy, Columbia University, Pupin Physics Laboratories, New York, NY 10027, USA

⁷ Institute for Computational Science, University of Zurich, Winterthurerstrasse 190, CH-8057 Zurich, Switzerland

⁸ Department of Physics and Astronomy, Rutgers University, 136 Frelinghuysen Road, Piscataway, NJ 08854, USA

⁹ Department of Physics, University of North Texas, Denton, TX 76203, USA

¹⁰ Center for Interdisciplinary Exploration and Research in Astrophysics (CIERA) and Department of Physics and Astronomy, Northwestern University, 1800 Sherman Avenue, Evanston, IL 60201, USA

Received 2022 August 22; revised 2023 April 14; accepted 2023 April 21; published 2023 June 16

Abstract

We present a suite of high-resolution simulations of an isolated dwarf galaxy using four different hydrodynamical codes: GIZMO, AREPO, GADGET, and RAMSES. All codes adopt the same physical model, which includes radiative cooling, photoelectric heating, star formation, and supernova (SN) feedback. Individual SN explosions are directly resolved without resorting to subgrid models, eliminating one of the major uncertainties in cosmological simulations. We find reasonable agreement on the time-averaged star formation rates as well as the joint density–temperature distributions between all codes. However, the Lagrangian codes show significantly burstier star formation, larger SN-driven bubbles, and stronger galactic outflows compared to the Eulerian code. This is caused by the behavior in the dense, collapsing gas clouds when the Jeans length becomes unresolved: Gas in Lagrangian codes collapses to much higher densities than that in Eulerian codes, as the latter is stabilized by the minimal cell size. Therefore, more of the gas cloud is converted to stars and SNe are much more clustered in the Lagrangian models, amplifying their dynamical impact. The differences between Lagrangian and Eulerian codes can be reduced by adopting a higher star formation efficiency in Eulerian codes, which significantly enhances SN clustering in the latter. Adopting a zero SN delay time reduces burstiness in all codes, resulting in vanishing outflows as SN clustering is suppressed.

Unified Astronomy Thesaurus concepts: [Galaxy formation \(595\)](#); [Stellar feedback \(1602\)](#); [Hydrodynamical simulations \(767\)](#)

1. Introduction

Tremendous progress has been made in hydrodynamical simulation of galaxy formation in the last decade (see Somerville & Davé 2015 and references herein). Starting with initial conditions from the cosmic microwave background, the simulated galaxies evolving across the cosmic time are remarkably realistic in many aspects, such as their masses, sizes, metallicities, colors, morphologies, etc. These simulations provide crucial information that is often observationally inaccessible and therefore have routinely been used to study the physical processes that shape the observed galaxies.

However, galaxy formation is fundamentally a multiscale problem that spans several orders of magnitude both spatially and temporally. The computational cost of simulating the relevant dynamical range is impractically high and will remain so in the foreseeable future. Therefore, phenomenological subgrid models are required to account for the physical processes on unresolved scales with several tunable parameters,

rendering their predictive power somewhat ambiguous (see Naab & Ostriker 2017 and references therein).

On the other hand, small-scale simulations have provided valuable insights from a “bottom-up” perspective (Walch et al. 2015; Girichidis et al. 2016; Ibáñez-Mejía et al. 2016; Gatto et al. 2017; Li et al. 2017; Kim & Ostriker 2017, 2018; Kim et al. 2020; Hu et al. 2021). These simulations focus on a patch of the interstellar medium (ISM) on kiloparsec scales and therefore can achieve much higher resolution, following the turbulence and gravitational collapse that shapes the multiphase ISM down to much smaller scales and higher densities. More importantly, feedback from supernova (SN) explosions can be faithfully modeled when the energy-conserving Sedov–Taylor phase is resolved, which requires a spatial resolution of ~ 4 pc in Eulerian codes (Kim & Ostriker 2015; Simpson et al. 2015) or a mass resolution of $\sim 10 M_{\odot}$ in Lagrangian codes (Hu 2019; Steinwandel et al. 2020) under typical ISM conditions. The difficulty in resolving SN feedback in cosmological simulations is a long-standing problem and has motivated a plethora of subgrid models. Dramatically different simulation results arise primarily from the differences in the adopted feedback prescriptions while the differences in the hydrodynamical techniques only play a secondary role (e.g., Scannapieco et al. 2012). Resolving SN feedback therefore eliminates a major source of uncertainty.



Original content from this work may be used under the terms of the [Creative Commons Attribution 4.0 licence](#). Any further distribution of this work must maintain attribution to the author(s) and the title of the work, journal citation and DOI.

However, the periodic boundary conditions adopted in ISM-patch simulations place a fundamental limitation on their applicability on large scales such as the lack of spiral waves (Smith et al. 2020) and potentially unrealistic behavior in galactic outflows (Martizzi et al. 2016).

Recently, galaxy-scale simulations that can resolve individual SN feedback in an isolated galaxy have become feasible (Forbes et al. 2016; Hu et al. 2016, 2017; Smith et al. 2018, 2021; Hu 2019; Emerick et al. 2019; Gutcke et al. 2021; Smith 2021; Hislop et al. 2022). They have more realistic boundary conditions than the ISM-patch simulations and can accurately capture the large-scale properties. Dwarf galaxies, thanks to their small sizes, are the primary targets for this type of simulation. More ambitious efforts have been made to pursue SN-resolved simulations of galaxy mergers (Lahén et al. 2019, 2020) or even SN-resolved cosmological “zoom-in” simulations (Wheeler et al. 2019; Agertz et al. 2020; Calura et al. 2022; Gutcke et al. 2022). Therefore, it is timely to design and perform simulations of a “typical” dwarf galaxy that can serve as a laboratory for code comparison and numerical experiments.

In this paper, as part of the SMAUG (Simulating Multiscale Astrophysics to Understand Galaxies) project,¹¹ we conduct simulations of an isolated dwarf galaxy using four different hydrodynamical codes with the same physical model. The SMAUG project aims at improving the predictive power of large-scale cosmological simulations by developing subgrid models based on small-scale simulations (rather than calibrated to reproduce observations). The goal of this paper is to investigate which predictions in our small-scale simulations are robust and also to understand when and how differences arise. The uniqueness of our work compared to previous code comparison projects such as AGORA (Kim et al. 2016) is that we do not use subgrid models for SN feedback as our resolution is able to resolve it directly. For the sake of comparison and interpretation, we have opted for the minimum complexity that can capture the essential physics. Our results are therefore subject to the caveat of the neglected physics, which we will discuss in detail in Section 4.

This paper is organized as follows. In Section 2, we introduce our numerical framework and the hydrodynamical codes. In Section 3, we present our simulation results, demonstrating the striking differences between Lagrangian and Eulerian codes in the burstiness of star formation, gas morphology, and galactic outflows as a result of SN clustering. In Section 4, we discuss the implications and limitations of our results and compare them with previous work. In Section 5, we summarize our results.

2. Numerical Methods

2.1. Hydrodynamical Codes

We use four different codes for gravity and hydrodynamics: one Eulerian code (RAMSES), one moving mesh code (AREPO), and two Lagrangian codes (GIZMO and GADGET-3), which we briefly describe as follows.

GADGET-3 (hereafter GADGET for short) (Springel 2005) is a particle-based code. Gravity is solved using a “tree code” (Barnes & Hut 1986) where short-range forces are calculated pairwise while long-range forces are approximated by the center of mass of a tree node. Since it is designed for collisionless N -body problems,

gravitational forces at small distances are reduced by softening, and different softening lengths can be used for different components, such as gas, stars, and dark matter. Hydrodynamics is solved by the smoothed particle hydrodynamics (SPH) method (Lucy 1977). We adopt the SPHGAL implementation in Hu et al. (2014) that includes several improvements over traditional SPH methods; these improvements include the pressure-energy formulation (Hopkins 2015), the Wendland kernel (Dehnen & Aly 2012), variable artificial viscosity and conduction (Price 2008; Cullen & Dehnen 2010), and the time-step limiter (Durier & Dalla Vecchia 2012). Both gravity and hydrodynamics solvers are Lagrangian in the sense that particles follow the motions of the gas, stars, and dark matter. The initial mass carried by each particle is conserved as there are no mass fluxes between particles.

GIZMO (Hopkins 2015) is a multimethod code built on the code GADGET, featuring the meshless Godunov method (Gaburov & Nitadori 2011) for hydrodynamics. We adopt the meshless finite-mass (MFM) method proposed by Hopkins (2015) in this work. In MFM, the simulation domain is divided into overlapping cells defined by the particle distribution and a kernel function with a finite support radius. The Riemann problem is solved at the interfaces between cells. The cells move with the gas so that the mass fluxes between cells are assumed to be zero. GIZMO adopts the same gravity solver as GADGET and is a Lagrangian code when the MFM solver is used.

AREPO (Springel 2010; Pakmor et al. 2016; Weinberger et al. 2020) uses a second-order accurate finite-volume scheme on an unstructured, moving mesh. The simulation domain is discretized by a Voronoi tessellation, and a Riemann problem is solved at the interfaces between cells to compute fluxes. The discrete set of mesh-generating points that define the tessellation is allowed to move with a velocity close to that of the local fluid (with small corrections to maintain cell regularity). The method is therefore pseudo-Lagrangian, as the moving mesh tends to minimize mass fluxes between cells, with the result that they roughly maintain a constant mass. However, these mass fluxes are nonzero (in contrast to GADGET and GIZMO). In the standard usage of the code, adopted here, a refinement (de-refinement) scheme is used to split (merge) cells in order to enforce a constant mass resolution within a factor of 2. AREPO adopts a gravity solver similar to those employed in GADGET and GIZMO.

RAMSES (Teyssier 2002) is an Eulerian code with octree-based adaptive mesh refinement (AMR). The N -body solver is based on the adaptive-particle-mesh method. The Poisson equation is solved using the multigrid method with Dirichlet boundary conditions at level boundaries (Guillet & Teyssier 2011). Hydrodynamics is solved using the MUSCL scheme, a second-order finite-volume Godunov method, and the HLLC Riemann solver. For RAMSES, we used here a quasi-Lagrangian refinement criterion based on a target mass common to all codes in this work. We use a box size of 450 kpc with a minimum level of refinement $\ell_{\min} = 8$ and a maximum level of refinement $\ell_{\max} = 16$ ($\ell_{\max} = 17$) for the low (high) resolution run, resulting in a maximum spatial resolution of 7 pc (resp. 3.5 pc).

The mesh in Eulerian codes is static by definition. The quasi-Lagrangian AMR leads to an adaptive spatial resolution down to a minimum cell size. In contrast, in both moving mesh and Lagrangian codes, the resolution elements follow the motions of the gas, leading to a smoothly (and, in principle, infinitely) adaptive spatial resolution with a constant or near-constant

¹¹ <https://www.simonsfoundation.org/flatiron/center-for-computational-astrophysics/galaxy-formation/smaug>

mass resolution. Despite being pseudo-Lagrangian, moving mesh codes share many properties with Lagrangian codes. For convenience, we will refer to GADGET, GIZMO, and AREPO as “Lagrangian codes” hereafter.

2.2. Initial Conditions

The initial conditions are generated with the MAKEDISKGA-LAXY code developed in Springel et al. (2005), which consists of a rotating disk galaxy embedded in a dark matter halo. The halo has a virial radius $R_{\text{vir}} = 45$ kpc and a virial mass $M_{\text{vir}} = 10^{10} M_{\odot}$, and it follows a Hernquist profile, which matches an NFW (Navarro et al. 1997) profile at small radii with the concentration parameter $c = 15$ and the spin parameter $\lambda = 0.035$. The baryonic mass fraction is 0.8%, out of which $10^7 M_{\odot}$ is in the stellar disk and $7 \times 10^7 M_{\odot}$ in the gaseous disk. Both the stellar and gaseous disks follow an exponential profile with a scale length of 1 kpc, which makes the central gas surface density $\Sigma_{\text{gas}} \sim 10 M_{\odot} \text{pc}^{-2}$. The stellar disk has a scale height of 1 kpc, while the vertical profile of the gaseous disk is such that it is in vertical hydrostatic equilibrium. The initial gas temperature is set to 10^4 K. The hydrogen mass fraction is $X_{\text{H}} = 0.76$. Our initial conditions resemble the Wolf–Lundmark–Melotte (WLM) galaxy, a nearby star-forming dwarf irregular galaxy that has multiwavelength observations (Leaman et al. 2012; Rubio et al. 2015; Mondal et al. 2018). The simulation is run for 1 Gyr for the Lagrangian codes and 0.5 Gyr for RAMSES due to computational cost.

For RAMSES and AREPO, it is necessary to set up a minimum density for numerical purposes, which is $n = 10^{-7} \text{cm}^{-3}$ uniformly distributed in the background. In contrast, there is no background gas in the halo for GIZMO and GADGET.

2.3. Numerical Resolution

For comparison purposes, we should, ideally, adopt the same resolution in both Lagrangian and Eulerian codes. However, Lagrangian codes have a fixed mass resolution and an adaptive spatial resolution while Eulerian codes are the opposite. Due to this intrinsic difference, there is no unique way of choosing the same resolution for both methods. In this work, we adopt a spatial resolution of $\Delta x = 7$ pc in the low-resolution model for the Eulerian code RAMSES. At this resolution, the thermal Jeans length can be resolved up to $n \sim 100 \text{cm}^{-3}$ assuming $T = 30$ K. Therefore, for the Lagrangian codes, we choose the gas particle mass m_{g} such that the smoothing length is comparable to Δx at $n = 100 \text{cm}^{-3}$, which translates to $m_{\text{g}} = 100 M_{\odot}$ in the low-resolution models. The gravitational softening for the baryons (i.e., gas, preexisting stars, and the stars formed in the simulation) is set to be $h_{\text{g}} = 10$ pc. The dark matter halo is resolved with a much coarser resolution with the particle mass $m_{\text{dm}} = 10^4 M_{\odot}$ and the gravitational softening $h_{\text{dm}} = 200$ pc. In the high-resolution models, we simply decrease all the spatial resolutions by a factor of 2 and the mass resolutions by 8. Table 1 summarizes the resolution-related parameters.

2.4. Radiative Cooling

We use the public GRACKLE library (Smith et al. 2017)¹² for radiative cooling, adopting its equilibrium cooling table without solving a chemistry network. The gas metallicity is $Z = 0.002$ ($0.1 Z_{\odot}$) and is constant throughout the simulation.

Table 1
Numerical Resolution

Resolution	m_{dm} ($10^2 M_{\odot}$)	m_{g} (M_{\odot})	h_{dm} (pc)	h_{g} (pc)	Δx (pc)
low	10	100	200	10	7
high	1.25	12.5	100	5	3.5

Note. m_{dm} : particle mass of dark matter. m_{g} : particle mass of gas. h_{dm} : gravitational softening length for dark matter. h_{g} : gravitational softening length for gas. Δx : cell size.

In addition, we include heating from the photoelectric effect. Following Bakes & Tielens (1994) and Wolfire et al. (2003), the photoelectric heating rate can be expressed as

$$\Gamma_{\text{PE}} = 1.3 \times 10^{-24} n \epsilon_{\text{PE}} G_0 Z_{\text{d}}' \text{ erg cm}^{-3} \text{ s}^{-1}, \quad (1)$$

where n is the hydrogen number density, ϵ_{PE} is the photoelectric heating efficiency, G_0 is the radiation strength in units of the Habing field (Habing 1968), and Z_{d}' is the dust-to-gas mass ratio relative to the Milky Way value ($\sim 1\%$). We adopt a constant ϵ_{PE} of 0.05 (see Appendix A) and $Z_{\text{d}}' = 0.1$, assuming a linear Z - Z_{d}' relationship.¹³ We assume G_0 scales linearly with the SFR surface density (Σ_{SFR}), normalized to the solar-neighborhood values of $G_0 = 1.7$ and $\Sigma_{\text{SFR}} = 2.4 \times 10^{-3} M_{\odot} \text{yr}^{-1} \text{kpc}^{-2}$. Since the SFR is unknown prior to the simulation, we use low-resolution simulations to empirically determine the photoelectric heating rate as a function of the galactocentric radius R :

$$\Gamma_{\text{PE}} = \Gamma_{\text{PE},0} \exp\left(\frac{R_{\text{c}} - \max(R, R_{\text{c}})}{R_{\text{c}}}\right), \quad (2)$$

where $\Gamma_{\text{PE},0} = 2.6 \times 10^{-27} \text{ erg s}^{-1}$ and $R_{\text{c}} = 0.4$ kpc. Our low-resolution experiments suggest that the results are insensitive to modest variations of Γ_{PE} (a factor of 3), which is consistent with Hu et al. (2017) and Smith et al. (2021).

2.5. Star Formation

We adopt the stochastic star formation recipe commonly used in simulations of galaxy formation. The local SFR is $\dot{\rho}_{*} = \epsilon_{\text{SF}} \rho_{\text{gas}} / t_{\text{ff}}$, where ρ_{gas} is the gas density, ϵ_{SF} is the star formation efficiency, and $t_{\text{ff}} \equiv \sqrt{3\pi / (32G\rho_{\text{gas}})}$ is the free-fall time, and G is the gravitational constant. We adopt $\epsilon_{\text{SF}} = 1\%$ as our fiducial choice, but we also explore $\epsilon_{\text{SF}} = 100\%$ in some models. Instead of adopting a density threshold for star formation, we allow star formation only to occur when the thermal Jeans length $L_{\text{J}} = \sqrt{\pi c_s^2 / (G\rho_{\text{gas}})} < L_{\text{J},0}$, where c_s is the sound speed and $L_{\text{J},0}$ is a predefined star formation threshold. We adopt $L_{\text{J},0} = \Delta x$ such that gas is eligible for star formation only when the Jeans length becomes unresolved as we can no longer follow the gravitational collapse faithfully (Truelove et al. 1997). For Lagrangian codes, this star formation criterion roughly corresponds to the density where the Jeans mass becomes unresolved (Bate & Burkert 1997).

Star particles are stochastically created based on the local SFR. In the Lagrangian codes, the gas resolution element is

¹³ Observations suggest that the linear relationship between Z and Z_{d}' breaks down at low metallicity (Rémy-Ruyer et al. 2014). However, its impact on the thermal balance in the ISM can be rather small if heating from SN feedback dominates over photoelectric heating (Hu et al. 2016, 2017).

¹² <https://grackle.readthedocs.io/>

Table 2
Overview of Simulation Models

Model Name	Code	Resolution	ϵ_{SF}	t_{SN} (Myr)	Additional Comments
<i>gizmo_lr</i>	GIZMO	100 M_{\odot}	1%	10	
<i>arepo_lr</i>	AREPO	100 M_{\odot}	1%	10	
<i>gadget_lr</i>	GADGET	100 M_{\odot}	1%	10	
<i>ramses_lr</i>	RAMSES	7 pc	1%	10	
<i>gizmo</i>	GIZMO	12.5 M_{\odot}	1%	10	
<i>arepo</i>	AREPO	12.5 M_{\odot}	1%	10	
<i>ramses</i>	RAMSES	3.5 pc	1%	10	
<i>gizmo_tsn0</i>	GIZMO	12.5 M_{\odot}	1%	0	
<i>arepo_tsn0</i>	AREPO	12.5 M_{\odot}	1%	0	
<i>gadget_tsn0</i>	GADGET	12.5 M_{\odot}	1%	0	
<i>ramses_tsn0</i>	RAMSES	3.5 pc	1%	0	
<i>ramses_tsn50</i>	RAMSES	3.5 pc	1%	50	
<i>gizmo*</i>	GIZMO	12.5 M_{\odot}	1%	10	$t_{\text{SN}} = 0$ until $t = 0.25$ Gyr
<i>arepo*</i>	AREPO	12.5 M_{\odot}	1%	10	$t_{\text{SN}} = 0$ until $t = 0.25$ Gyr
<i>gadget*</i>	GADGET	12.5 M_{\odot}	1%	10	$t_{\text{SN}} = 0$ until $t = 0.25$ Gyr
<i>gizmo_sfe100</i>	GIZMO	12.5 M_{\odot}	100%	10	
<i>arepo_sfe100</i>	AREPO	12.5 M_{\odot}	100%	10	
<i>ramses_sfe100</i>	RAMSES	3.5 pc	100%	10	

Note. Models with an asterisk are run with $t_{\text{SN}} = 0$ for the first 0.25 Gyr to prevent the initial artificial blowout of the gaseous disk. ϵ_{SF} : star formation efficiency. t_{SN} : SN delay time.

converted into a star particle that inherits the mass of its parent. This means that all star particles in GADGET and GIZMO have a mass of m_{g} exactly, while star particles in AREPO are guaranteed to have a mass within a factor of 2 of m_{g} . In RAMSES, a star particle with a mass of m_{g} is spawned by removing a gas mass of m_{g} from the parent cell.

2.6. Supernova Feedback

We include feedback from core-collapse SNe. For a typical stellar population, there is about one SN progenitor in every 100 M_{\odot} stellar mass. As our star particle has a mass of $m_{*} \leq 100 M_{\odot}$, there is at most one SN progenitor in each star particle statistically. Therefore, we stochastically sample massive stars such that each star particle has a probability of $m_{*}/(100 M_{\odot})$ of being selected as an SN progenitor with an SN delay time of $t_{\text{SN}} = 10$ Myr. Each SN injects 10^{51} erg of thermal energy into the surrounding ISM. For RAMSES and AREPO, the energy is injected into the cell where the star is located. For GIZMO and GADGET, multiple cells can overlap with the same star simultaneously. For simplicity, we inject energy into the nearest eight particles in a kernel-weighted fashion. For each SN event, we record not only the ambient gas density and temperature but also the location and time such that we can perform a cluster analysis in Section 3.4.

2.7. Models

The models we run are summarized in Table 2. For the low-resolution case, we only run our fiducial model where $\epsilon_{\text{SF}} = 1\%$ and $t_{\text{SN}} = 10$ Myr. For the high-resolution case, we run our fiducial model, a model with $t_{\text{SN}} = 0$, and a model with $\epsilon_{\text{SF}} = 100\%$. For RAMSES, we run an additional model with $t_{\text{SN}} = 50$ Myr. Finally, we run a model for the Lagrangian codes (GIZMO, AREPO, and GADGET), where we adopt $t_{\text{SN}} = 0$ up to $t = 250$ Myr and $t_{\text{SN}} = 10$ Myr afterward. As we will demonstrate, this particular setup turns out to be our favored fiducial model for Lagrangian codes as it prevents the artificial blowout of

the disk during the initial phase. We do not have the GADGET runs for all the models (i.e., there is no *gadget* and *gadget_sfe100*).

3. Results

3.1. Star Formation Rate

Figure 1 shows the star formation rate (SFR) as a function of time for the low- and high-resolution models in the top and bottom panels, respectively. The average SFRs in the low-resolution models are in broad agreement in all codes. However, the *ramses_lr* model is notably less bursty (i.e., the SFR varies less with time) than the Lagrangian models. In addition, there is an initial starburst in the Lagrangian models at $t \sim 100$ Myr that is absent in the *ramses_lr* model. In the high-resolution models (bottom panel), the SFRs in the Lagrangian models become even burstier. Indeed, the initial starburst leads to extremely energetic SN feedback, which blows out the entire gaseous disk. Although a quasi-steady state is eventually established after some of the blown-out gas falls back, the overall gas surface density becomes significantly lower than that in the initial conditions, leading to a reduced time-averaged SFR. The blowout is, however, a somewhat artificial consequence of our initial conditions and numerical setup. Before the first star formation occurs, gas cools and collapses globally into an artificially thin disk. Once the gas becomes dense enough to form stars, the resulting coherent SNe can easily break out of the thin disk, resulting in a catastrophic blowout. This is a well-known phenomenon in simulations of isolated galaxies as well as in ISM patches, and several methods have been adopted to mitigate the initial blowout, such as turbulent driving (e.g., Walch et al. 2015; Kim & Ostriker 2017) or random SN driving (e.g., Hu et al. 2017; Smith et al. 2021). On the other hand, the *ramses* model still shows a nonbursty SFR similar to its low-resolution counterpart and there is no initial blowout of the disk, in sharp contrast to the Lagrangian models.

An important clue in understanding this difference comes from the observation that the SN delay time has a significant effect on the burstiness of star formation in the Lagrangian codes. The top panel of Figure 2 shows the SFR time evolution

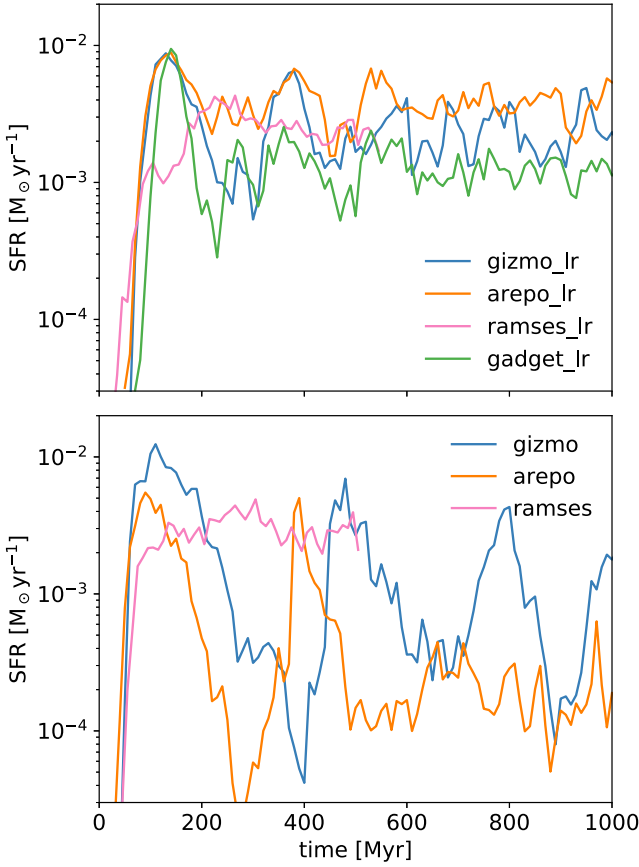


Figure 1. Star formation rate (SFR) as a function of time. Top: low-resolution models. Bottom: high-resolution models (there is no corresponding GADGET run). The SFR is much more bursty in the high-resolution runs in *gizmo* and *arepo* while it remains unchanged in *ramses*.

for models with instantaneous SN feedback ($t_{\text{SN}} = 0$). With this change, the SFRs in *gizmo_tsn0*, *ramses_tsn0*, and *gadget_tsn0* all show excellent agreement with each other. The SFR in *arepo_tsn0* is lower by a factor of 2, and it is unclear what causes the slight difference. More importantly, the SFRs in all codes are strikingly constant with little temporal fluctuation. In addition, the initial burst is absent and a quasi-steady state is rapidly established without the blowout of the disk.

An interesting implication is that instantaneous SN feedback can be a simple alternative method to mitigate the artificial initial starburst. Motivated by this, we rerun our Lagrangian codes with $t_{\text{SN}} = 0$ for $t < 250$ Myr and $t_{\text{SN}} = 10$ Myr for $t \geq 250$ Myr. We do not do so with RAMSES as it shows no initial starburst. The results are shown in the middle panel of Figure 2. The Lagrangian models show reasonable agreement with each other. Although there is still a burst of SFR at $t \gtrsim 250$ Myr right after we switch t_{SN} from 0 to 10 Myr, it is much weaker and does not blow out the disk. Consequently, the time-averaged SFR is not reduced and is comparable to *ramses*. We therefore refer to these models as our “fiducial” Lagrangian models. However, even if the artifacts of the initial conditions have been greatly reduced, the SFRs for the Lagrangian codes are still burstier than *ramses*. This suggests that the difference in burstiness between the two methods is an intrinsic property rather than an artifact of the initial conditions.

The observed SFR in the WLM galaxy from Hunter et al. (2010) is $1.7 \times 10^{-3} M_{\odot} \text{yr}^{-1}$ from H α and $6.3 \times 10^{-3} M_{\odot} \text{yr}^{-1}$ from far-ultraviolet (FUV). The SFRs in our

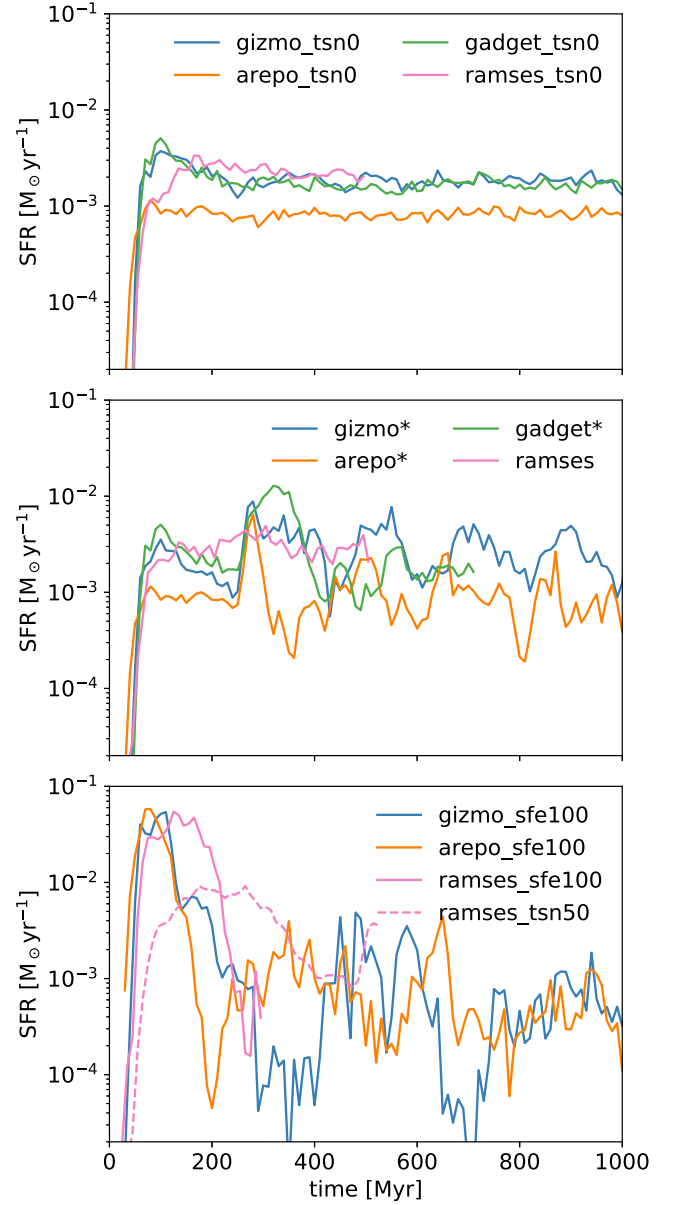


Figure 2. Same as Figure 1 but for the rest of the high-resolution models. Top: models with instantaneous SN feedback ($t_{\text{SN}} = 0$). The SFR is nonbursty in all codes. Middle: Lagrangian models with $t_{\text{SN}} = 0$ until $t = 250$ Myr (*gizmo**, *arepo**, and *gadget**) in order to mitigate the initial artificial starburst. The Lagrangian codes are still more bursty than *ramses* at $t \geq 250$ Myr. Bottom: models with $\epsilon_{\text{SF}} = 100\%$ (solid lines) and a RAMSES model with $t_{\text{SN}} = 50$ Myr (*ramses_tsn50*, dashed line). Increasing either ϵ_{SF} or t_{SN} makes the SFR in RAMSES more bursty, similar to the Lagrangian models.

fiducial models are broadly in good agreement with observations, which is reassuring.

The bottom panel of Figure 2 shows models with $\epsilon_{\text{SF}} = 100\%$ as well as a RAMSES model with $t_{\text{SN}} = 50$ Myr. Both *gizmo_sfe100* and *arepo_sfe100* show very bursty SFRs similar to the corresponding models *gizmo* and *arepo* where $\epsilon_{\text{SF}} = 1\%$. On the other hand, both *ramses_sfe100* and *ramses_tsn50* are bursty, in contrast to *ramses*. In other words, the burstiness in Eulerian codes can be enhanced by increasing either ϵ_{SF} or t_{SN} . We will explore the reason for this in later sections.

The time-averaged SFRs of different models are summarized in Table 3.

Table 3
Summary of Simulation Results

Model Name (1)	Initial Blowout (2)	Clustered SNe (3)	$\langle \text{SFR} \rangle$ (4)	$\langle \eta_m \rangle$ (5)	$\langle \eta_e \rangle$ (6)
<i>gizmo</i>	yes	yes	1.2	3.0	0.041
<i>arepo</i>	yes	yes	0.39	19	1.1
<i>ramses</i>	no	no	3.1	0.17	0.0015
<i>gizmo_tsn0</i>	no	no	1.8	0.011	5.6×10^{-5}
<i>arepo_tsn0</i>	no	no	0.82	0.0017	3.3×10^{-6}
<i>ramses_tsn0</i>	no	no	2.2
<i>gadget_tsn0</i>	no	no	1.7	0.032	8.1×10^{-5}
<i>gizmo*</i>	no	yes	3.1	1.1	0.015
<i>arepo*</i>	no	yes	1.1	5.4	0.15
<i>gadget*</i>	no	yes	3.4	4.3	0.27
<i>gizmo_sfe100</i>	yes	yes	0.66	16	0.25
<i>arepo_sfe100</i>	yes	yes	0.85	7.6	0.29
<i>ramses_sfe100</i>	yes	yes	0.53	13	0.49
<i>ramses_tsn50</i>	yes	yes	3.1	3.2	0.10

Note. (4) Time-averaged SFR in units of $10^{-3} M_{\odot} \text{ yr}^{-1}$. (5) Time-averaged mass-loading factor. (6) Time-averaged energy-loading factor. The first 250 Myr is excluded from the time-averaging to discard the initial transient phase.

3.2. Gas Morphology and Thermal State

Figure 3 shows the face-on maps of the gas surface density in different models at $t = 500$ Myr. The most striking feature is that large SN-driven bubbles are clearly seen in some models but are completely absent in others. In fact, the presence of SN bubbles is closely correlated with the burstiness of the SFR shown in Figures 1 and 2: Models with burstier star formation show larger SN bubbles. In particular, those that experience an initial blowout have the largest SN bubbles, and their gas surface densities are notably reduced even at $t = 500$ Myr, as some of the blown-out gas never falls back to the disk. On the other hand, SN bubbles are completely absent in models where $t_{\text{SN}} = 0$. Similarly, the standard *ramses* runs show very few SN bubbles, consistent with its nonbursty star formation history. SN bubbles in RAMSES models can only be generated by increasing either ϵ_{SF} (*ramses_sfe100*) or t_{SN} (*ramses_tsn50*).

Figure 4 shows the two-dimensional mass-weighted normalized distribution of the hydrogen number density versus temperature (the so-called “phase diagram”) at $t = 500$ Myr. The red solid line indicates the star formation threshold where $L_J = 3.5$ pc. Broadly speaking, all models show similar distributions in the phase diagram despite their differences in star formation burstiness and gas morphology. This is because the thermal balance in the ISM is mainly controlled by radiative cooling. The majority of gas is in the diffuse warm gas, where $n \sim 0.1 \text{ cm}^{-3}$ and $T \sim 10^4$ K, which is consistent with Hu et al. (2016, 2017). However, models with $t_{\text{SN}} = 0$ produce less hot ($T > 10^5$ K) and diffuse gas compared to their fiducial counterparts. This is expected as the hot and diffuse gas typically exists in the SN bubbles that are largely absent in these models. The RAMSES runs have more gas in the density range of $n \sim 10\text{--}100 \text{ cm}^{-3}$ as indicated by the slightly brighter color but have very little gas above the star formation threshold.

3.3. Environments for Supernovae and Star Formation

The environment where SNe occur provides crucial information on the efficiency of SN feedback. The left panel of Figure 5 shows the cumulative distribution of the ambient gas density where SNe occur (n_{SN}) for the Lagrangian models. The agreement between different Lagrangian codes is remarkable. Most SNe occur in diffuse gas where $n_{\text{SN}} \sim 10^{-2} \text{ cm}^{-3}$ in the

fiducial models (*gizmo**, *arepo**, and *gadget**) and therefore are well resolved. In contrast, most SNe occur in dense gas where $n_{\text{SN}} \sim 10^2 \text{ cm}^{-3}$ in the instantaneous SN models (*gizmo_tsn0*, *arepo_tsn0*, and *gadget_tsn0*). This is expected, as SN feedback kicks in right after star formation, which by construction only occurs in cold and dense gas,¹⁴ leading to more efficient energy loss from radiative cooling, which explains the nonburstiness and the lack of SN bubbles. Although these SNe are formally unresolved, the time-averaged SFRs in these models are still comparable to those in the fiducial models, suggesting that these “unresolved” SNe are still able to inject enough momentum to regulate star formation.

In contrast, *ramses* shows a very different n_{SN} distribution compared to the Lagrangian codes with a significant fraction of SNe occurring at $n > 10 \text{ cm}^{-3}$, as shown in the right panel of Figure 5. This is part of the explanation for why *ramses* behaves more like the instantaneous SN models. However, there are still $\sim 25\%$ of SNe with $n_{\text{SN}} < 0.01 \text{ cm}^{-3}$ in *ramses*, which is not significantly lower compared to *gizmo**. This implies that SNe occurring at low densities is not a sufficient condition for efficient feedback, which we will discuss in more detail in Section 3.4. On the other hand, both *ramses_sfe100* and *ramses_tsn50* have a large fraction of low- n_{SN} SNe and therefore show busy SFRs and large SN bubbles.

Having established that the burstiness and gas morphology are both related to n_{SN} , we now need to understand what leads to the difference in n_{SN} in different models.

The left panel of Figure 6 shows the cumulative distribution of the gas density where star formation occurs (n_{SF}) for the Lagrangian codes. The agreement between different Lagrangian codes is again remarkable. With instantaneous SN feedback (dashed lines), most star formation occurs in a narrow range of densities where $n \sim 500 \text{ cm}^{-3}$. Once the gas reaches high enough densities to form stars, SN feedback that occurs instantaneously is able to stop the gas from further collapsing. Therefore, stars always form around the star

¹⁴ We note that *arepo_tsn0* is implemented in a way that the SN delay time is very small but not exactly zero. This explains why its cumulative distribution of n_{SN} is not exactly the same as that of n_{SF} but is instead slightly shifted to lower values, which might explain the factor of 2 difference in the SFR in Figure 2.

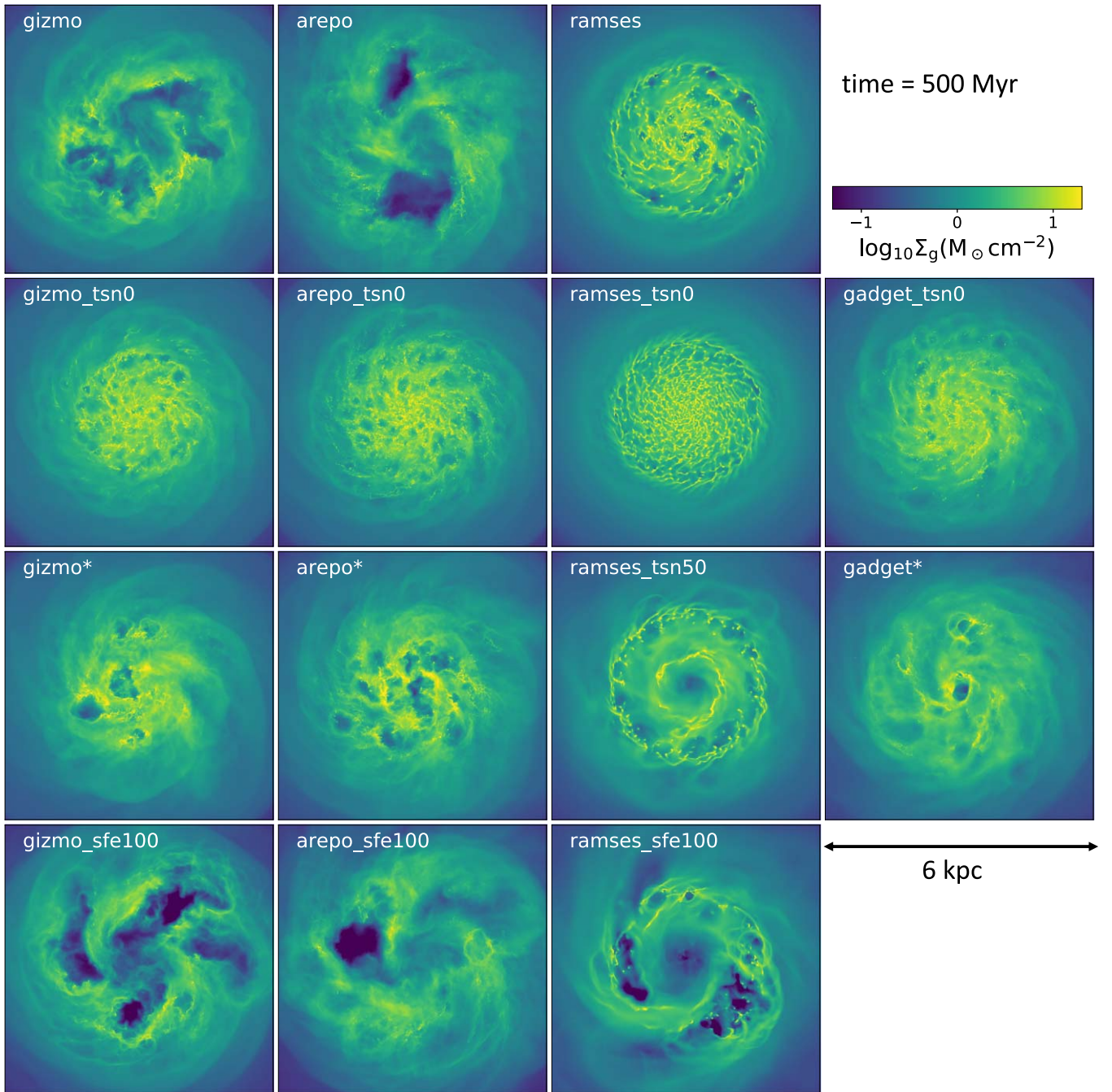


Figure 3. Gas surface density in the face-on view in different models at $t = 500$ Myr. The SN-driven bubbles are clearly visible in most cases except in models with $t_{\text{SN}} = 0$ and in *ramses*.

formation threshold density. In contrast, in the fiducial models with $t_{\text{SN}} = 10$ Myr (solid lines), star formation occurs over a large range of densities, spanning more than two orders of magnitude from 500 to 10^5 cm^{-3} . In this case, gas keeps collapsing toward higher densities even after it exceeds the threshold density, as there is no countering mechanism against gravity before the first SNe occur in 10 Myr. In contrast, as shown in the right panel of Figure 6, *ramses* behaves very differently from its Lagrangian counterparts, showing a narrow range of n_{SF} very similar to the instantaneous SN models.

We therefore conclude that Lagrangian and Eulerian codes behave very differently at densities above the star formation

threshold where the Jeans length becomes unresolved: While gas in Lagrangian codes continues to collapse to much higher (unresolved) densities, gas in Eulerian codes lingers around the star formation threshold. This is because the spatial resolution in Lagrangian codes is adaptive and therefore it is much easier for the unresolved gas to collapse. In comparison, the collapse of unresolved gas in Eulerian codes is limited by the fixed spatial resolution and is thus relatively more difficult. Note that in both cases, the collapse is unresolved (and additional physical processes such as pre-SN feedback may become important) and so neither behavior is necessarily correct.

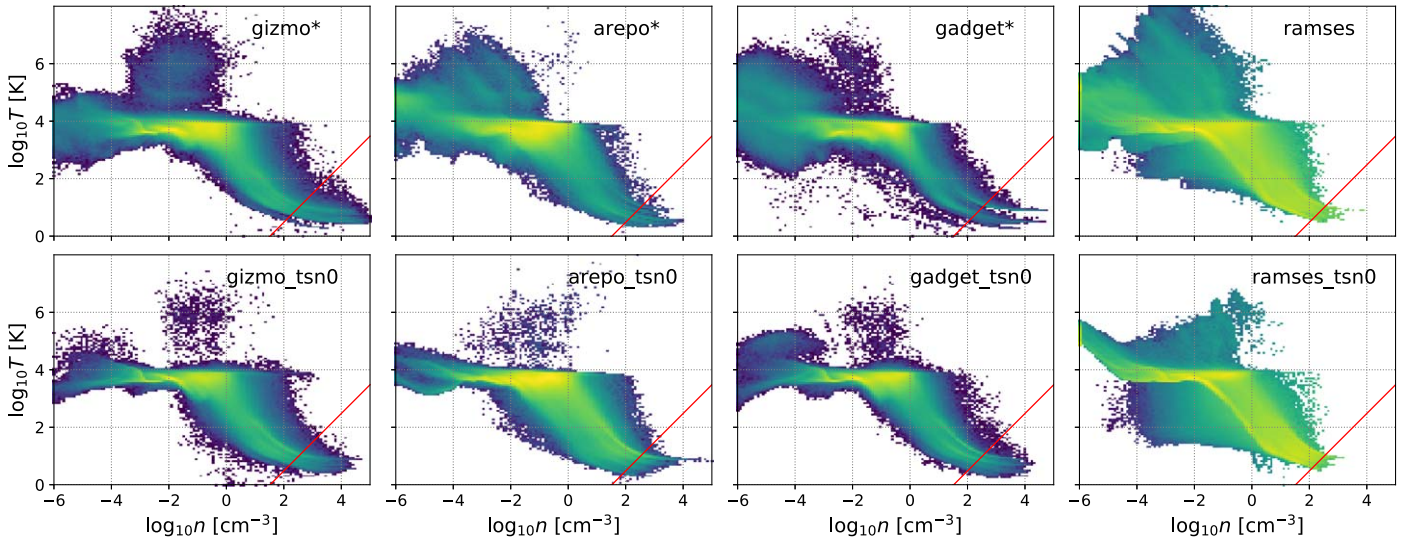


Figure 4. Two-dimensional mass-weighted normalized distribution of the hydrogen number density (n) vs. temperature (T) at $t = 500$ Myr. The red solid line indicates the star formation threshold where the Jeans length $L_J = 3.5$ pc. All models show broadly similar distributions, though models with $t_{\text{SN}} = 0$ produce less hot and diffuse gas compared to their fiducial counterparts.

3.4. Supernova Clustering

In this section, we study the clustering properties of SNe and show that SN clustering has a fundamental impact on n_{SN} , SFR burstiness, and gas morphology. The effect of SN clustering is two-fold. First, it reduces the ambient gas densities such that the SN bubble will retain the overpressurized hot gas for a longer time as the radiative cooling rate becomes lower than the energy injection rate of the temporally clustered SNe (Gatto et al. 2015; Kim & Ostriker 2015; Walch et al. 2015; Girichidis et al. 2016; Gentry et al. 2017). Second, it generates coherent gas flows with less momentum cancellation. Therefore, it facilitates the formation of large SN bubbles that can break out of the gaseous disk (Kim et al. 2017; Orr et al. 2022).

The SN clusters are defined by the friends-of-friends method following Smith et al. (2021). This is possible as we record the location and time of each SN event in the simulations. In addition to a linking length of 10 pc, we also impose a linking time of 1 Myr to ensure that the SNe are indeed temporally clustered. The number of SNe in each SN cluster is defined as the clustering number N_{cl} . We perform the analysis in the “lab” frame and do not correct for the effect of galactic rotation. This means that an SN might drift away from the SN cluster it physically belongs to by more than a linking length due to rotation and thus it would be incorrectly excluded. We argue that this should only be a minor effect as most of our SNe are temporally clustered at much shorter timescales than 1 Myr (see Figure 10).

Figure 7 shows the spatial distributions of the top 10 SN clusters (ranked by N_{cl}) in different models. Each point represents an SN event, and different colors represent different SN clusters. The average clustering number of the top 10 SN clusters $\langle N_{\text{cl}} \rangle$ is shown in each panel.

Comparing the fiducial models, *gizmo** and *arepo** show significantly more clustered SNe than *ramses*, with $\langle N_{\text{cl}} \rangle$ larger by about an order of magnitude. In Lagrangian codes, as gas is able to collapse to densities far above the threshold density, star formation is locally enhanced due to the $\rho_{\text{g}}^{1.5}$ dependency. This makes the SNe highly clustered, which collectively generates large SN bubbles and low n_{SN} , and leads to bursty star formation. The significantly less clustered SNe in *ramses*

suggests that having a low n_{SN} , as we showed in Figure 5, is not a guarantee for efficient feedback—the SNe have to be clustered, too. Meanwhile, the location of SNe in *gizmo** and *arepo** closely follows the trajectory of galactic rotation, implying that the SN progenitors rarely drift away from their birth clouds and explode in the diffuse medium, which is a potential cause for the low n_{SN} . This is perhaps not surprising as we do not resolve the collisional stellar dynamics and neither do we include any subgrid treatment for the so-called “runaway” or “walkaway” stars (de Mink et al. 2014).

To further support our argument that strong SN clustering is indeed caused by locally enhanced SFR, we conduct another numerical experiment, presented in Appendix B, where we force the local SFR to scale linearly rather than superlinearly with gas density. In this case, despite the formation of dense clouds, star formation in the clouds proceeds slowly, resulting in low clustering of SNe and an attendant lack of burstiness (resulting in inefficient outflows—see the following section). In this way, the Lagrangian code behaves similarly to the fiducial *Ramses* model despite using the fiducial SN delay time of 10 Myr, emphasizing that the root difference is tied ultimately to SN clustering.

On the other hand, the instantaneous SN models (*gizmo_tsn0*, *arepo_tsn0*, and *ramses_tsn0*) represent the extreme case where SN clustering is strongly suppressed. Once star formation occurs, SN feedback immediately stops any further gravitational collapse and the development of any subsequent SNe. This leads to high n_{SN} and thus more rapid energy loss, as well as smaller SN-driven bubbles, resulting in a weaker dynamical impact on the ISM.

With $\epsilon_{\text{SF}} = 100\%$, SNe are highly clustered in all models. The Lagrangian codes show a similar level of SN clustering compared to their fiducial counterparts (where $\epsilon_{\text{SF}} = 1\%$). The lack of clusters in the central area of *arepo_sfe100* is caused by its strong initial blowout. As opposed to the *ramses* model, *ramses_sfe100* shows significantly more clustered SNe, with $\langle N_{\text{cl}} \rangle$ larger by a factor of 30, consistent with its low n_{SN} , bursty SFR, and large SN bubbles.

Figure 8 shows N_{cl} as a function of the median time of the SNe in a cluster (t_{cl}) in the *gizmo** model. Each circle represents an SN cluster. The effect of the SN delay time on clustering is

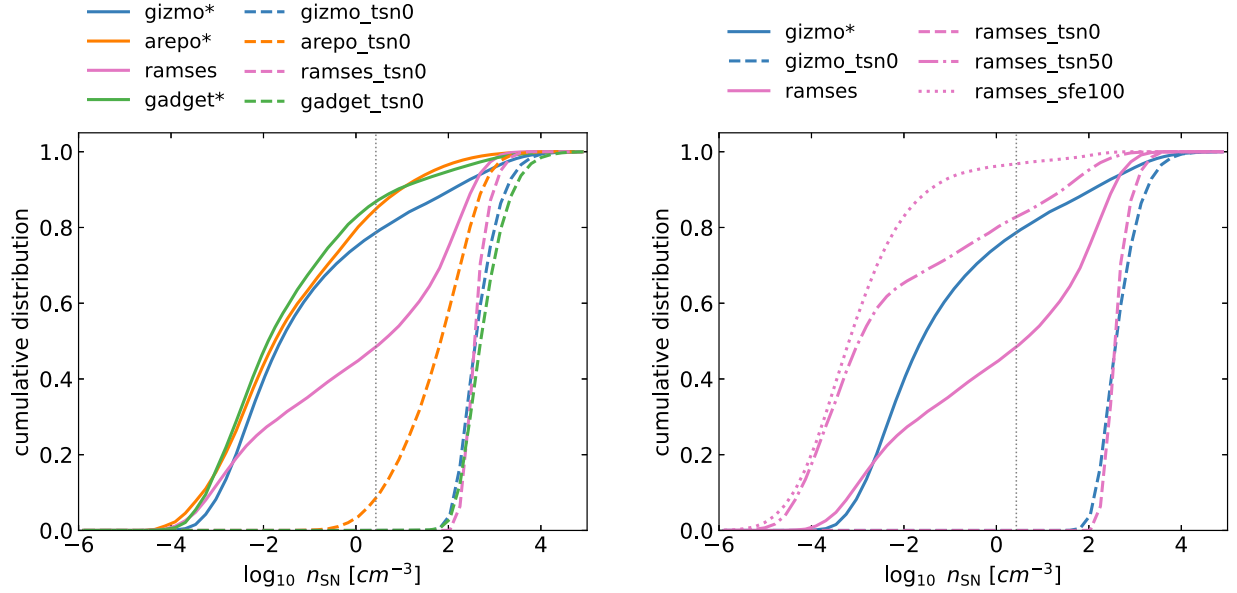


Figure 5. Cumulative distribution of the ambient density where SNe occur (n_{SN}). The vertical dotted line indicates the density above which the SN cooling radius becomes unresolved. Left: fiducial and instantaneous SN models in Lagrangian codes. Most SNe occur in diffuse gas where $n_{\text{SN}} \sim 10^{-2} \text{ cm}^{-3}$ in the fiducial models while most SNe occur in dense gas where $n_{\text{SN}} \sim 10^2 \text{ cm}^{-3}$ in models where $t_{\text{SN}} = 0$. The agreement between different Lagrangian codes is remarkable. Right: comparison between Lagrangian (GIZMO) and Eulerian (RAMSES) models. The fiducial RAMSES model (*ramses*) shows a significantly lower fraction of SNe occurring in diffuse gas than *gizmo**. Increasing either ϵ_{SF} or t_{SN} in RAMSES greatly increases the probability of SNe occurring in diffuse gas.

clearly demonstrated: once t_{SN} is switched from 0 to 10 Myr at $t = 250$ Myr (indicated by the vertical dashed line), SNe immediately become significantly clustered.

To demonstrate the development of SN bubbles, Figure 9 shows the SN ambient temperature (T_{SN} , left panel) and density (right panel) as a function of the normalized time ($t - t_{\text{cl}}$) for the top four SN clusters (ranked in N_{cl}) in the *gizmo** model. Each point represents an SN event and different colors and symbols represent different clusters. All of these clusters share a similar time evolution: the first SNe occur in cold and dense gas, which gradually heat up and evacuate the gas, eventually saturating at $T_{\text{SN}} \sim 10^8 \text{ K}$ and $n_{\text{SN}} \sim 10^{-3} \text{ cm}^{-3}$.

To quantify the environmental properties of SN clusters, we calculate the median of the ambient temperature (T_{cl}) and density (n_{cl}) of each SN cluster as a function of N_{cl} in Figure 10. The solid line shows the median values of T_{cl} or n_{cl} in each N_{cl} bin while the shaded area brackets the 25th and 75th percentiles. For *gizmo_tsn0* and *arepo_tsn0*, SNe are forced to occur in cold and dense gas by construction. In contrast, in both *gizmo* and *arepo*, as N_{cl} increases, T_{cl} increases while n_{cl} decreases. At $N_{\text{cl}} > 20$, T_{cl} becomes higher than 10^5 K , indicating the development of hot gas in the SN bubbles, which has been shown to be critical for launching galactic outflows (Walch et al. 2015; Girichidis et al. 2016; Hu 2019).

3.5. Galactic Outflows

Galactic outflows driven by SNe play a critical role in galaxy formation. We characterize the outflows in a similar fashion as in Hu (2019). We define the mass outflow rate as

$$\dot{M}_{\text{out}} = \sum_i \frac{m_{\text{g},i} v_{z,i}}{\Delta z} \quad (3)$$

and the energy outflow rate as

$$\dot{E}_{\text{out}} = \sum_i \frac{m_{\text{g},i} (v_i^2 + \gamma u_i) v_{z,i}}{\Delta z}, \quad (4)$$

where v_i is the gas velocity, $v_{z,i}$ is the gas velocity along the vertical direction, $\gamma = 5/3$ is the adiabatic index, u_i is the specific internal energy, and $\Delta z = 0.1 \text{ kpc}$ is the thickness of the plane where outflows are measured. Here $z = 0$ corresponds to the midplane of the disk in the initial conditions. The summation is over cells or particles that are (i) located between $z = 10 \pm 0.5 \Delta z \text{ kpc}$ or $z = -10 \pm 0.5 \Delta z \text{ kpc}$ and (ii) traveling “outward,” i.e., $z_i v_{z,i} > 0$.

We define the mass-loading factor,

$$\eta_{\text{m}} \equiv \frac{\dot{M}_{\text{out}}}{\langle \text{SFR} \rangle}, \quad (5)$$

and the energy-loading factor,

$$\eta_{\text{e}} \equiv \frac{M_{\text{SN}} \dot{E}_{\text{out}}}{E_{\text{SN}} \langle \text{SFR} \rangle}, \quad (6)$$

where $E_{\text{SN}} = 10^{51} \text{ erg}$ is the injection energy per SN and $M_{\text{SN}} = 100 M_{\odot}$ is the corresponding mass formed in a stellar population per SN. The bracket $\langle \dots \rangle$ represents time-averaging, and we exclude $t < 250 \text{ Myr}$ to discard the initial transient phase. We use the time-averaged SFR instead of the instantaneous SFR as the normalization factor such that the fluctuations of η_{m} and η_{e} are purely due to the fluctuations in the outflows. The time-averaged η_{m} and η_{e} , summarized in Table 3, are therefore $\langle \eta_{\text{m}} \rangle = \langle \dot{M}_{\text{out}} \rangle / \langle \text{SFR} \rangle$ and $\langle \eta_{\text{e}} \rangle = M_{\text{SN}} \langle \dot{E}_{\text{out}} \rangle / (E_{\text{SN}} \langle \text{SFR} \rangle)$, respectively.

Figure 11 shows \dot{M}_{out} (top panel) and \dot{E}_{out} (bottom panel) as a function of time across the planes of $z = \pm 10 \text{ kpc}$ for the Lagrangian models. Instantaneous SN models have more than two orders of magnitude lower outflow rates compared to the fiducial models, demonstrating that SN clustering substantially enhances outflows. Both *gadget_tsn0* and *gizmo_tsn0* show weak but nonzero outflows at $t \sim 100 \text{ Myr}$ as a result of the initial star formation, which is absent in *arepo_tsn0*. This is

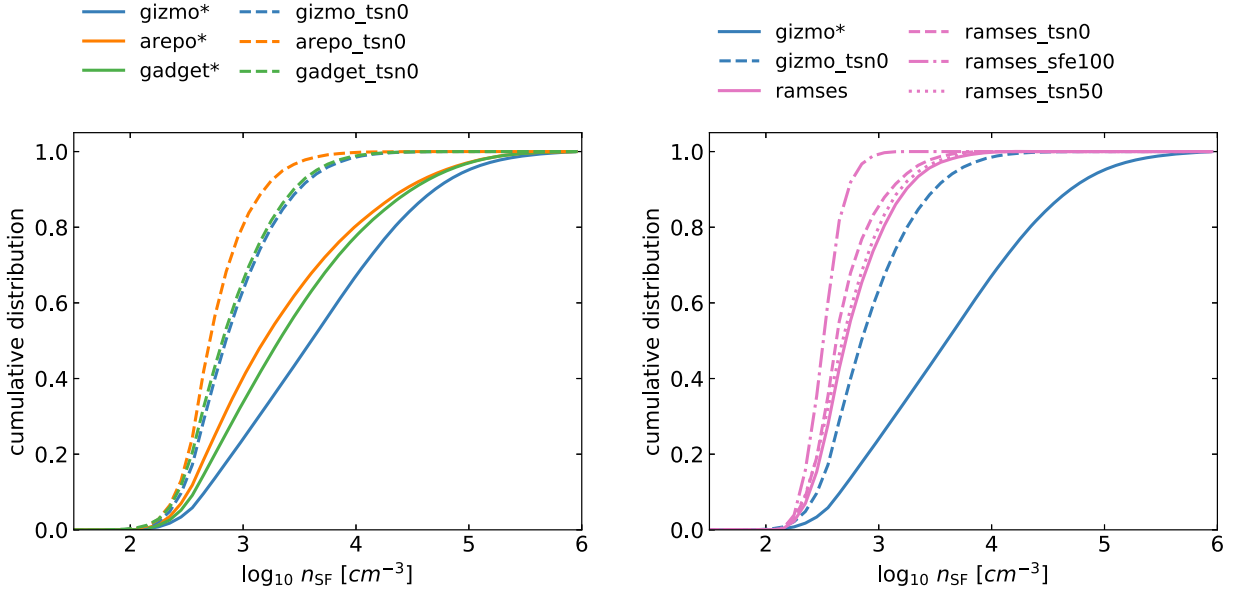


Figure 6. Same as Figure 5 but for the ambient density where star formation occurs (n_{SF}). In Lagrangian codes, gas collapses way beyond the star formation threshold density in the fiducial models. In contrast, star formation mostly occurs around the threshold density in all RAMSES models.

likely due to the difference in the initial conditions: *arepo_tsn0* includes a low-density background for numerical purposes while *gadget_tsn0* and *gizmo_tsn0* adopt a vacuum background that presumably facilitates the relatively weak outflows to expand and fill up the vacuum.

Interestingly, the outflow rates in the fiducial models show notable differences even though their SFRs, n_{SN} , and n_{SF} are all in good agreement. The difference between *arepo** and *gadget** is mostly due to their SFRs, which differ by a factor of 3, while their $\langle\eta_{\text{m}}\rangle$ and $\langle\eta_{\text{e}}\rangle$ only differ by a factor of 25% and 80%, respectively. However, *gizmo** is a factor of 4–5 lower in $\langle\eta_{\text{m}}\rangle$ and a factor of 10–18 lower in $\langle\eta_{\text{e}}\rangle$ compared to *arepo** and *gadget**. The origin of this difference is still unclear and requires further investigation in future work.

We now compare outflows between Eulerian and Lagrangian codes in Figure 12. For clarity, we only show the AREPO models as a representation of Lagrangian codes. The *ramses* model is a factor of 32 lower in $\langle\eta_{\text{m}}\rangle$ and a factor of 100 lower in $\langle\eta_{\text{e}}\rangle$ compared to *arepo**, reflecting the fact that SNe are significantly more clustered in *arepo**. The outflow rates in RAMSES are enhanced with either a larger t_{SN} or a larger ϵ_{SF} , as both would increase the SN clustering. Indeed, *ramses_tsn50* and *ramses_sfe100* both show comparable outflow rates with *arepo**.

We conclude that SN clustering plays a fundamental role in driving galactic outflows. Only models with significant SN clustering show $\langle\eta_{\text{m}}\rangle$ larger than unity.

4. Discussion

4.1. Comparison with Previous Works

Several recent studies have quantified outflows in terms of η_{m} and η_{e} in similar initial conditions of a dwarf galaxy with resolved SN feedback. Our fiducial Lagrangian models (*gizmo**, *arepo**, and *gadget**) are in broad agreement with these studies: Hu (2019) found $\langle\eta_{\text{m}}\rangle \sim 4$ and $\langle\eta_{\text{e}}\rangle \sim 0.07$ at $|z| = 10$ kpc using the GADGET code. Smith et al. (2021) found η_{m} fluctuating between 1 and 10 and η_{e} between 0.003 and 0.3 at $|z| = 10$ kpc in a comparable model (their *PE-SN*) using the AREPO code. Gutcke et al. (2021) found η_{m} between 5 and 10 and η_{e} between 10^{-4} and 10^{-3} at $|z| = 2$ kpc in a comparable

model (their *FIXED_SN_ENERGY*) using the AREPO code. We note that η_{m} is in better agreement among these studies than η_{e} , probably because η_{e} is very sensitive to small differences in the gas velocity (see Equation (4)). Our results confirm these previous findings that the predicted η_{m} from SN-resolved galaxy-scale simulations are significantly lower than what cosmological simulations commonly assume in their subgrid models. Observations of nearby dwarf galaxies seem to support the low- η_{m} case (McQuinn et al. 2019).

In a similar setup, Hu et al. (2017) found that a shortened SN delay time ($t_{\text{SN}} = 3$ Myr) has the effect of suppressing the formation of SN bubbles and galactic outflows, which is consistent with our results. However, they did not find an effect of t_{SN} on the burstiness of star formation. Smith et al. (2021) showed that photoionization from massive stars prior to the SN events (the so-called “early feedback”) reduces SN clustering and thus significantly suppresses the burstiness of star formation, formation of SN bubbles, and galactic outflows, reducing η_{m} and η_{e} by more than an order of magnitude. This is very similar to our instantaneous SN models, which can be viewed as an extreme case of early feedback. Keller & Kruijssen (2022) simulated a Milky Way–like galaxy with $m_{\text{g}} \sim 10^5 M_{\odot}$, where SN feedback is modeled in a subgrid fashion. Although the simulated galaxy and the numerical treatments are very different, they found that a longer SN delay time enhances galactic outflows by enhancing the clustering of young stars, which is qualitatively consistent with our results.

Kim et al. (2016) have conducted a detailed code comparison study for an isolated Milky Way–like galaxy with significantly more participating codes. They found that different codes generally agree well with each other. In particular, they did not find systematic differences between Lagrangian and Eulerian codes in terms of burstiness and the sizes of SN bubbles. This is probably because they have adopted the simple thermal injection as their subgrid prescription for SN feedback, which is known to be very inefficient at this resolution as most energy would be radiated away without generating much momentum.

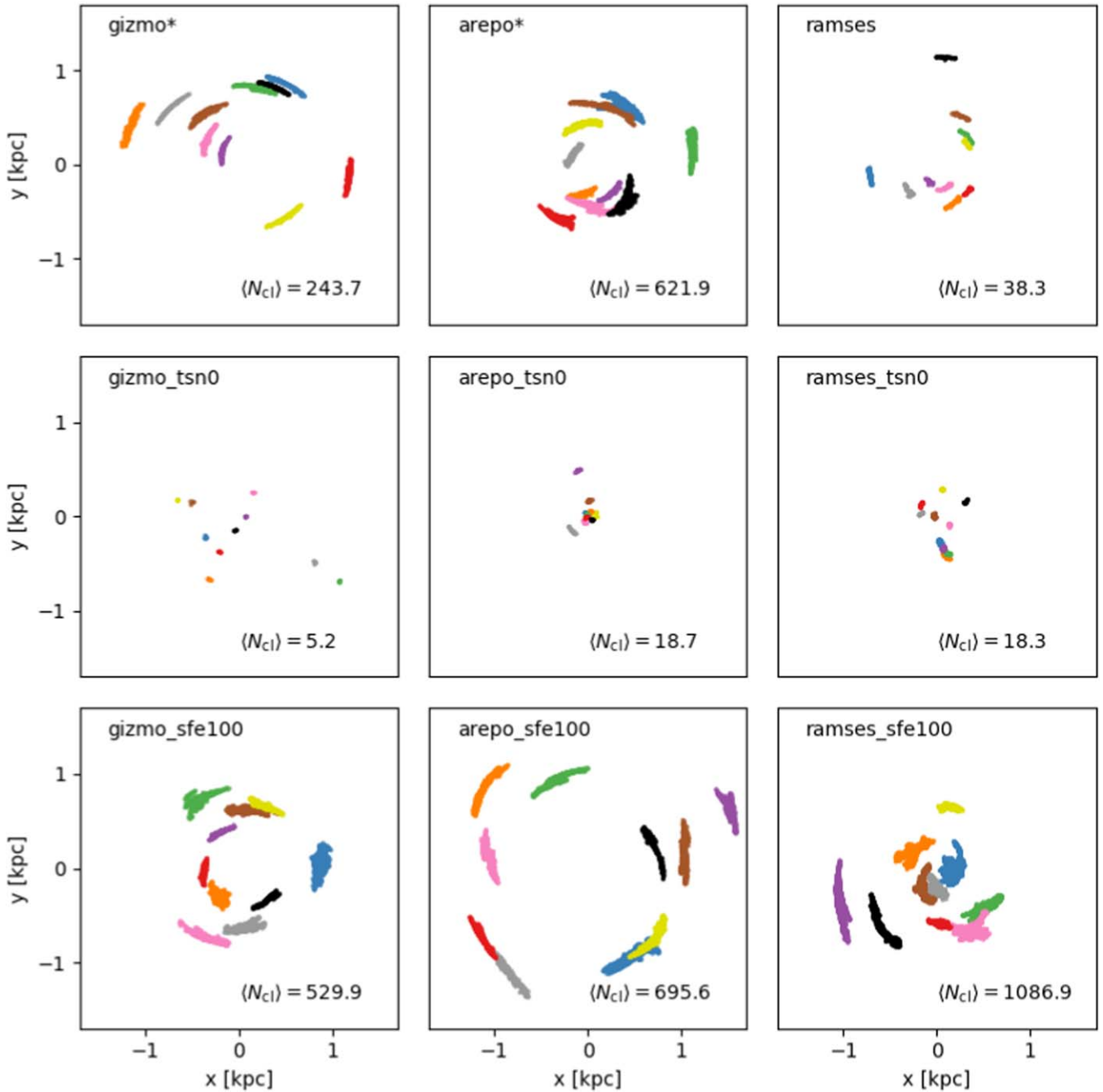


Figure 7. Top 10 SN clusters (ranked by the clustering number N_{cl}) in each model in the face-on view. Each circle represents an SN event while each color represents an SN cluster. The average clustering number of the top ten clusters is shown as $\langle N_{cl} \rangle$. SNe are significantly less clustered in models with $t_{SN} = 0$ as well as in the fiducial RAMSES model (*ramses*).

4.2. Differences between Numerical Methods

As we have shown in Section 3.3, the differences between Lagrangian and Eulerian codes arise near the resolution limit when the Jeans length becomes unresolved. This is perhaps not surprising: Code differences almost by definition have to occur near the resolution limit, as the resolved scales should converge to the physical solutions for any numerically consistent method. However, in our case, the differences at the resolution limit quickly propagate to much larger, well-resolved scales due to clustered star formation and SN feedback.

As we alluded to in Section 3.3, once the gas enters the Jeans length-unresolved regime, both methods can no longer faithfully

follow the collapse, and the evolution of gas depends sensitively on numerics such as gravitational softening. That said, it is interesting to ask which method is “less wrong.” For a collapsing cloud that becomes unresolved, both the Jeans mass and Jeans length would keep decreasing as the density increases. In other words, the cloud should keep collapsing and fragmenting. Lagrangian codes cannot capture the fragmentation without particle splitting or cell refinement, and they might underestimate the collapsing speed if the adopted softening length is much larger than the cell size. However, the cloud will continue to collapse as expected. In contrast, the collapse in an Eulerian code would halt when the Jeans length becomes unresolved as it requires accreting

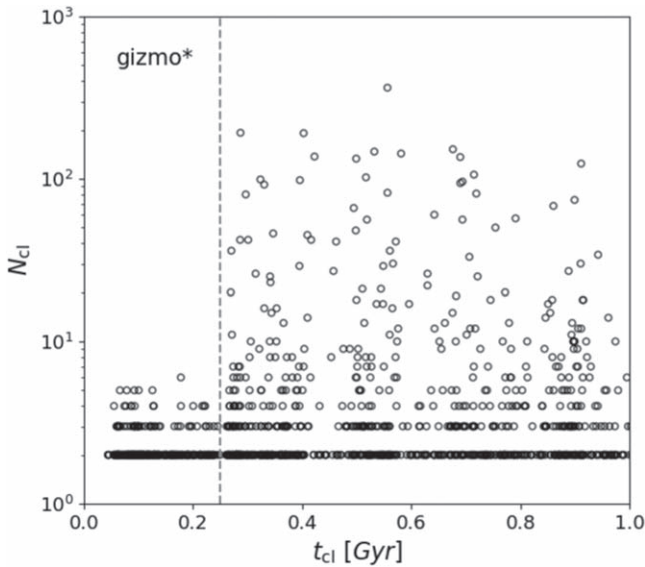


Figure 8. SN clustering number (N_{cl}) as a function of the median time of the SNe in a cluster (t_{cl}) in the model *gizmo**. Each circle represents an SN cluster. The vertical dashed line indicates the time when t_{SN} is switched from 0 to 10 Myr, which leads to a substantial increase in N_{cl} .

gas into the minimum cell. In this sense, Lagrangian codes are arguably more accurate than Eulerian codes in the unresolved regime.¹⁵

The situation becomes more subtle if we consider the physical processes we do not include in this work. In particular, as we do not include feedback from photoionization, we might have overestimated SN clustering and more significantly so in our Lagrangian models. If this is the case, our Eulerian model would more accurately, though coincidentally, predict the SN clustering.

4.3. Star Formation Efficiency

Previous studies have shown that the star formation efficiency only has a weak effect on the galaxy-scale SFR in both Lagrangian and Eulerian codes (e.g., Agertz et al. 2013; Benincasa et al. 2016; Semenov et al. 2017; Hopkins et al. 2018). While this is consistent with our Lagrangian models, it appears to be in conflict with our Eulerian models where increasing ϵ_{SF} leads to a qualitative change in the burstiness of star formation due to enhanced SN clustering. This is probably because SN feedback is unresolved and treated in a subgrid fashion in those studies, which reduces its dynamical impact. Alternatively, as those studies simulated more massive galaxies, the local burstiness might have been averaged out such that the global SFR remains the same. In this case, we expect the outflow rates to increase with ϵ_{SF} .

Instead of assuming a constant ϵ_{SF} , some recent simulations of galaxy formation have adopted a class of subgrid models for star formation that calculates ϵ_{SF} based on local gas properties (Semenov et al. 2016; Kretschmer & Teyssier 2020). These models assume a subgrid log-normal density distribution as predicted by simulations of supersonic turbulence, and models differ in their criteria for the onset of star formation (Krumholz & McKee 2005; Hennebelle & Chabrier 2008; Padoan & Nordlund 2011; Federrath & Klessen 2012; Burkhardt 2018;

Burkhart & Mocz 2019). Our results suggest that adopting such a subgrid model would have a much stronger effect on Eulerian codes as they are more sensitive to the variation of ϵ_{SF} .

4.4. Numerical Convergence

The significant differences between our low- and high-resolution models suggest that we have not yet reached numerical convergence. This is consistent with Smith et al. (2018) whose models with $m_g = 20 M_\odot$ and $m_g = 200 M_\odot$ still show significantly different outflow rates. In addition, the convergence study in Hu (2019) with $m_g = 1, 5, 25,$ and $125 M_\odot$ showed that convergence was only achieved at $m_g = 5 M_\odot$ when individual SNe are properly resolved. Therefore, we optimistically expect that our high-resolution models are actually close to convergence.

Many recent cosmological “zoom-in” simulations have adopted an SN feedback model that injects thermal energy for resolved SNe and injects the terminal momentum for unresolved SNe as a subgrid model (e.g., Hopkins et al. 2014, 2018; Agertz & Kravtsov 2015; Kimm et al. 2015; Marinacci et al. 2019). Most of these simulations have resolutions much coarser than our low-resolution models, suggesting that their SN feedback still operates in the subgrid regime where galactic outflows are expected to be underestimated due to the lack of hot gas (Hu 2019). More recent studies such as Agertz et al. (2020), Gutcke et al. (2022), and Calura et al. (2022) have started to resolve individual SNe in cosmological “zoom-in” simulations of dwarf galaxies, which is a promising way forward.

4.5. Missing Physics and Future Prospects

The main caveat of our results is the fact that we do not include pre-SN feedback such as photoionization. As we already discussed, this could lead to overestimated SN clustering, in particular for our Lagrangian models. This is a potential solution for the discrepancies we find between the two types of methods. An interesting follow-up project is therefore to include photoionization and see if the discrepancies can be mitigated. On the other hand, the suppression of SN clustering by photoionization in Smith et al. (2021) could also have been overestimated by the adopted “Strömgren-type” approach where dense clumps are preferentially ionized. Interestingly, Rathjen et al. (2021) conducted ISM-patch simulations using radiative transfer based on an inverse ray-tracing technique and reached the same conclusion that photoionization suppresses SN clustering, which leads to less efficient hot gas generation. This should be investigated by future galaxy-scale simulations using more accurate methods of radiative transfer such as adaptive ray tracing (Emerick et al. 2019). We note that including a solver for radiative transfer does not necessarily resolve the issue, as the important part is to ensure sufficient angular resolution to prevent the dense clumps from being preferentially ionized. This therefore implies a very demanding computational cost.

Another potentially important element is the collisional stellar dynamics. While we adopt a collisionless gravity solver in this work, the stellar dynamics in young star clusters is actually collisional. As our results highlight the importance of SN clustering, it is desirable to include an accurate N -body integrator, such as in Wall et al. (2020) and Rantala et al. (2021), to properly follow the evolution of young star clusters. However, the computational feasibility of incorporating it into galaxy-scale simulations remains to be explored. On the other hand, stellar

¹⁵ Eulerian codes might behave more similarly to Lagrangian codes when adopting a minimum cell size well below the resolvable Jeans length. However, this would be prohibitively expensive in practical applications.

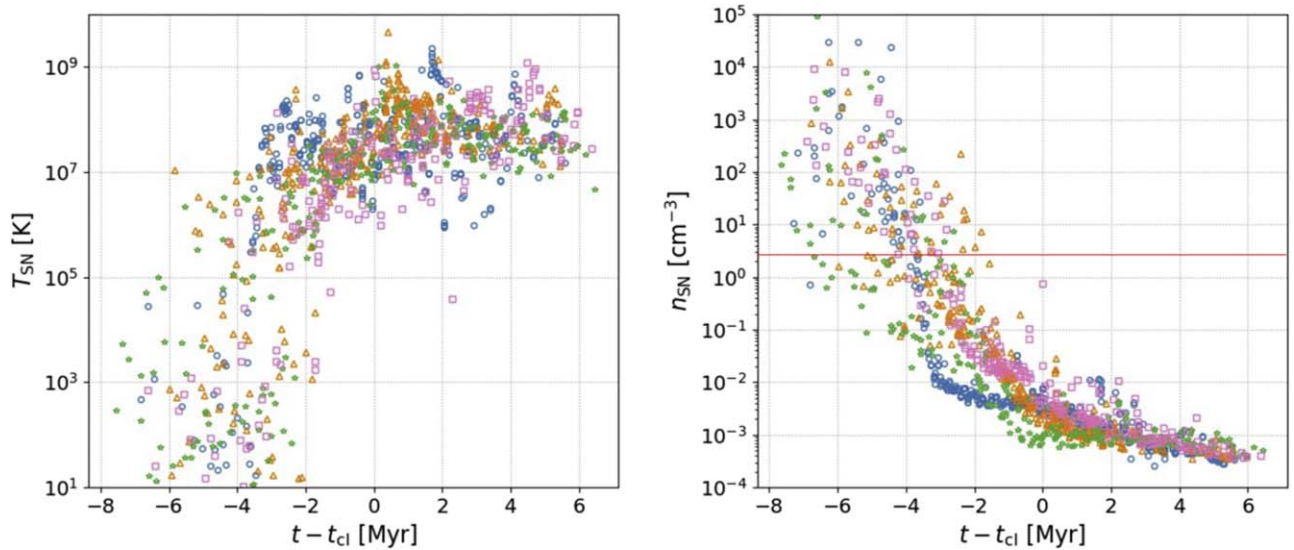


Figure 9. SN ambient temperature (T_{SN} , left) and density (n_{SN} , right) as a function of the normalized time ($t - t_{\text{cl}}$) for the top four SN clusters (ranked by N_{cl}) in the *gizmo** model. Each point represents an SN event and different colors and symbols represent different clusters. The horizontal red line indicates the density above which the SN cooling radius becomes unresolved. The first SNe occur in cold and dense gas, which heat up and evacuate the gas, and the subsequent SNe occur in increasingly hot and diffuse gas.

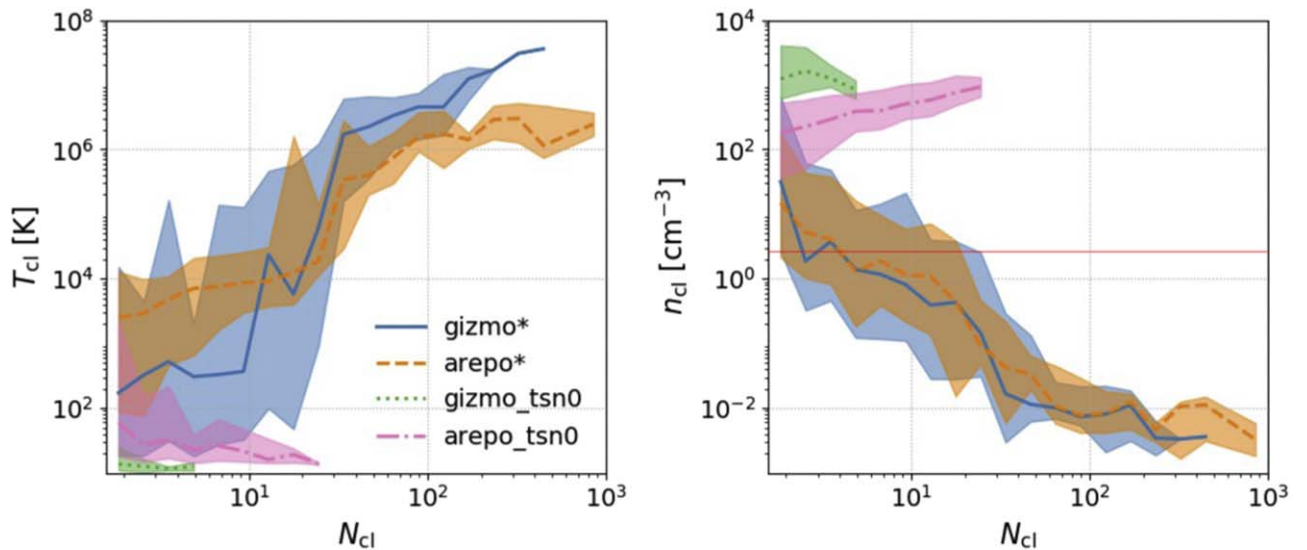


Figure 10. Left: median SN ambient temperature of a cluster (T_{cl}) as a function of N_{cl} . The solid line shows the median values in each N_{cl} bin while the shaded area brackets the 25th and 75th percentiles. Right: same as the left but for the median SN ambient density n_{cl} . The horizontal red line indicates the density above which the SN cooling radius becomes unresolved. Hot gas ($T > 10^5$ K) is generated when $N_{\text{cl}} \gtrsim 20$.

dynamics can be modeled in a subgrid fashion. Steinwandel et al. (2022) simulated a dwarf galaxy similar to ours, including a subgrid model for runaway massive stars that can enhance $\langle \eta_{\text{m}} \rangle$ by 50% and $\langle \eta_{\text{e}} \rangle$ by a factor of 5.

5. Summary

We have conducted a suite of simulations of an isolated dwarf galaxy using four different hydrodynamical codes (GIZMO, AREPO, GADGET, and RAMSES). All codes adopt the same physical model, which includes radiative cooling, photoelectric heating, star formation, and SN feedback. We directly resolve individual SN feedback without using subgrid models, which is a major source of uncertainty in cosmological simulations. Our main results can be summarized as follows.

1. The time-averaged SFRs and the distributions of gas density and temperature are in reasonable agreement in all codes (Table 3 and Figure 4). However, Lagrangian codes show a burstier star formation history (Figures 1 and 2), larger SN-driven bubbles (Figure 3), and stronger galactic outflows (Figures 11 and 12), in striking contrast to the Eulerian code. This originates from the different behaviors as gas collapses beyond the star formation threshold: the Jeans-length-unresolved gas collapses to much higher densities in the Lagrangian codes (Figure 6), leading to a more complete conversion of gas into stars and hence more highly clustered SNe (Figure 7). Hot gas ($T > 10^5$ K) in the SN bubbles that drives galactic outflows is generated when the SN clustering number is sufficiently high (Figure 10).

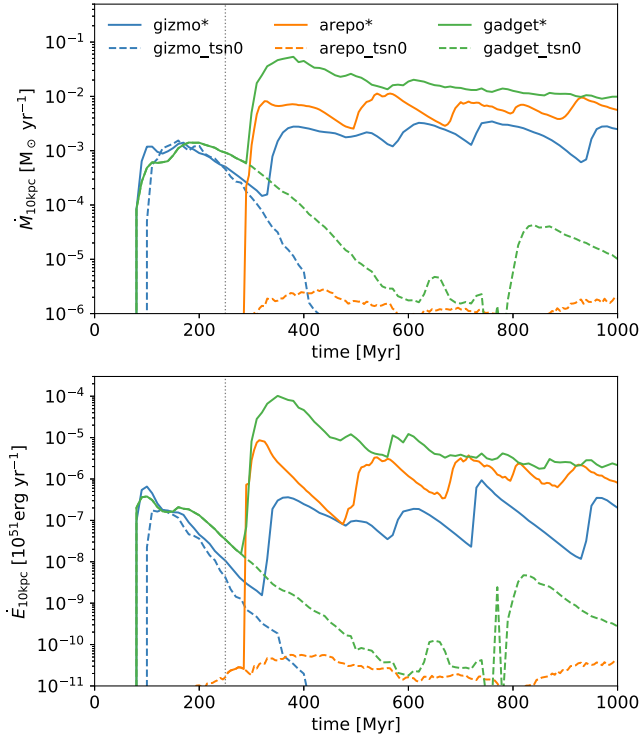


Figure 11. Mass (top panel) and energy (bottom panel) outflow rates as a function of time across the planes of $z = \pm 10$ kpc for the Lagrangian models. The vertical dotted line indicates $t = 250$ Myr. SN delay time has a significant impact on the outflow rates.

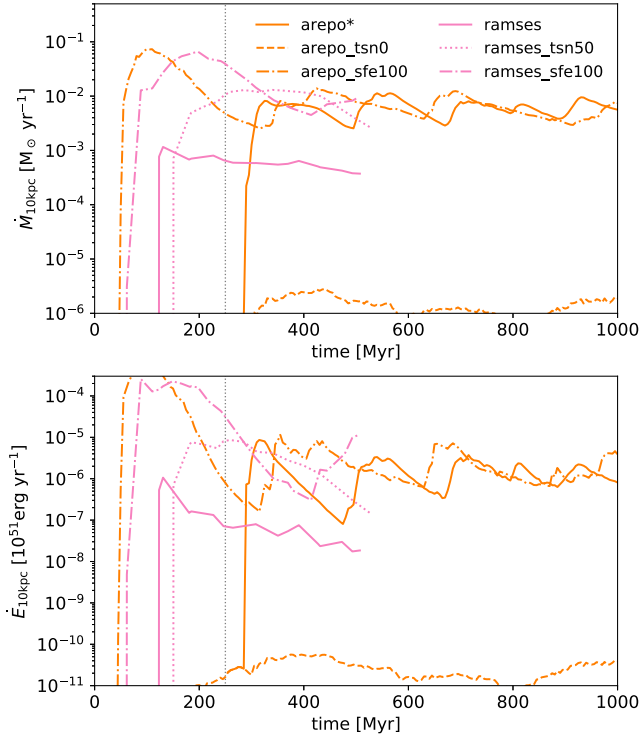


Figure 12. Same as Figure 11 but for the AREPO and RAMSES models.

2. If we let SN feedback occur with a zero delay time immediately after star formation as a numerical experiment, SN clustering would be strongly suppressed and SNe are forced to occur at high densities with rapid radiative losses. In this case, all codes behave similarly,

showing a nonfluctuating SFR, no visible SN bubbles, and vanishing galactic outflows.

3. The adopted star formation efficiency (ϵ_{SF}) has a significant effect on SN clustering in Eulerian codes, which in turn affects the star formation burstiness, sizes of SN bubbles, and outflow rates. In contrast, ϵ_{SF} only plays a minor role in Lagrangian codes where gas collapses to much higher densities such that local star formation is significantly enhanced, effectively enhancing ϵ_{SF} even when a low value is used.
4. Lagrangian models are in good agreement with each other in terms of gas morphology, SN densities, and star formation densities. However, GIZMO shows notably weaker outflows compared to AREPO and GADGET in the fiducial models, which requires further investigations in future work.

Acknowledgments

We thank the anonymous referee for the constructive comments that helped improve the manuscript, in particular for suggesting the additional run in Appendix B. We thank Volker Springel and Chang-Goo Kim for a stimulating discussion. C.Y.H. acknowledges support from the Deutsche Forschungsgemeinschaft (DFG, German Research Foundation) via German-Israel Project Cooperation grant STE1869/2-1 GE625/17-1 and NASA ATP grant 80NSSC22K0716. The work of MCS was supported by a grant from the Simons Foundation (CCA 668771, LEH) and by the DFG under Germany’s Excellence Strategy EXC 2181/1-390900948 (the Heidelberg STRUCTURES Excellence Cluster). The Center for Computational Astrophysics is supported by the Simons Foundation. G.L.B. acknowledges support from the NSF (AST-2108470, XSEDE), a NASA TCAN award, and the Simons Foundation through their support of the Learning the Universe Collaboration. B.B. thanks the Alfred P. Sloan Foundation and the Packard Foundation for support as well as the support of NASA grant No. 80NSSC20K0500. Y.L. acknowledges financial support from NSF grant AST-2107735 and NASA grant 80NSSC22K0668.

Appendix A Photoelectric Heating Efficiency

In this section, we investigate if our adopted constant photoelectric efficiency $\epsilon_{\text{PE}} = 0.05$ is a good approximation (see Equation (1)). In the upper-left panel of Figure 13, we show the gas temperature at thermal equilibrium as a function of density by running our adopted GRACKLE module for 1 Gyr at each density bin (green dotted line). The initial temperature is set at 10^4 K and the metallicity is $0.1 Z_{\odot}$. In comparison, we also show the equilibrium temperature as a function of density obtained by running the nonequilibrium chemistry code developed by Simon Glover (Glover & Mac Low 2007; Glover & Clark 2012) (hereafter SGCHEM) for 1 Gyr at each density bin: The solid blue line is with a cosmic-ray (CR) ionization rate $\zeta = 10^{-16} \text{ s}^{-1}$ motivated by H_3^+ observations in the Milky Way (Indriolo & McCall 2012) while the dashed orange line is with $\zeta = 0$.

The photoelectric efficiency adopted in SGCHEM is

$$\epsilon_{\text{PE}} = \frac{0.049}{1 + (0.004\psi)^{0.73}} + \frac{0.037(T/10000)^{0.7}}{1 + 2 \times 10^{-4}\psi}, \quad (\text{A1})$$

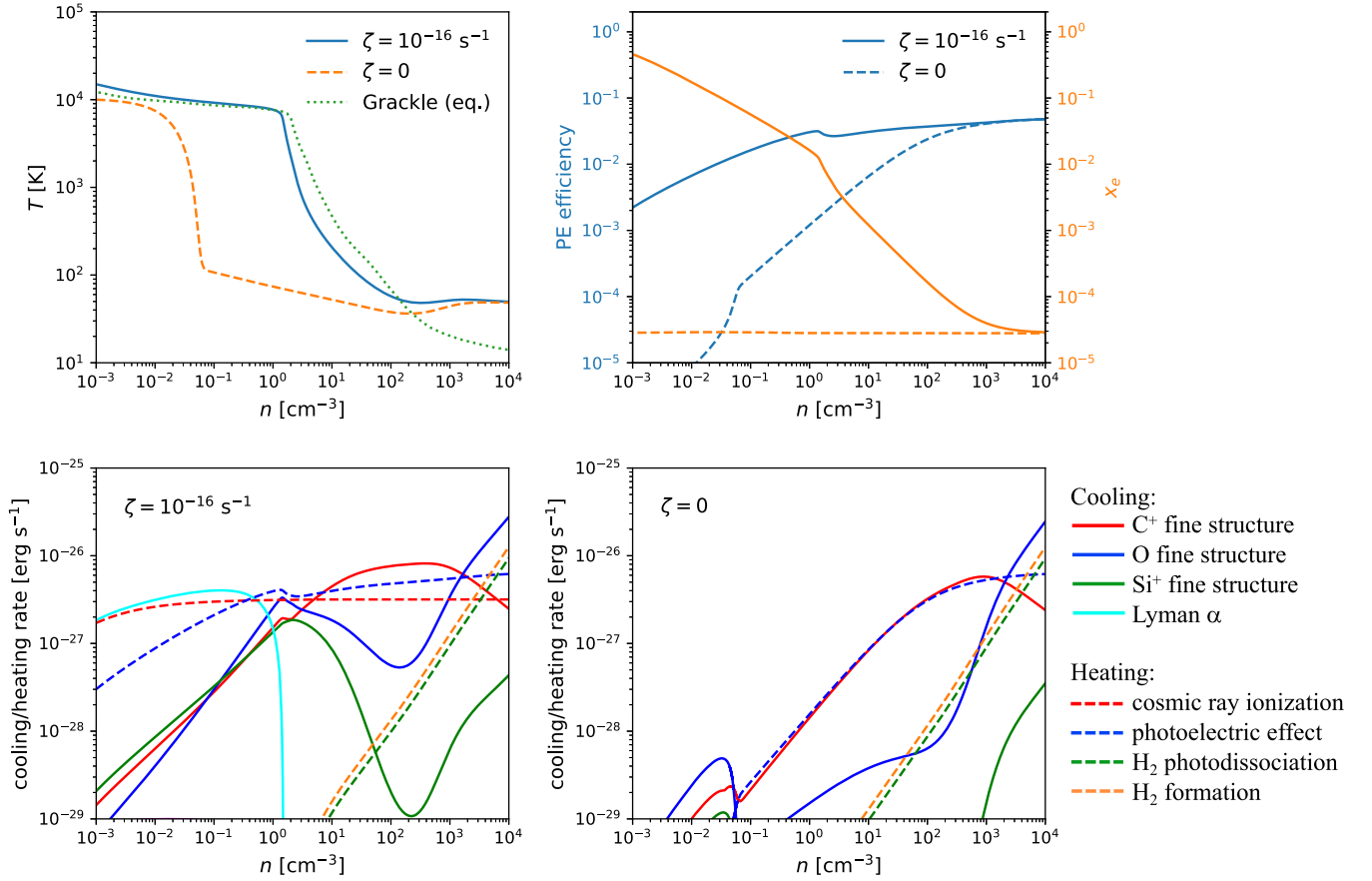


Figure 13. Upper left: equilibrium temperature as a function of density for the GRACKLE equilibrium module (dotted green), SGCHEM (see text) with cosmic-ray ionization rate $\zeta = 10^{-16} \text{ s}^{-1}$ (solid blue), and SGCHEM with $\zeta = 0$ (dashed orange). Upper right: photoelectric efficiency (ϵ_{PE} , blue) and electron abundance (x_e , orange) as a function of density for SGCHEM with $\zeta = 10^{-16} \text{ s}^{-1}$ (solid) and $\zeta = 0$ (dashed). Lower left: individual cooling and heating processes as a function of density in SGCHEM with $\zeta = 10^{-16} \text{ s}^{-1}$. Lower right: same as lower left, but with $\zeta = 0$. Adopting a constant ϵ_{PE} is a fair approximation of the more realistic situation where both the photoelectric effect and cosmic -ray ionization are present.

where $\psi = G_0 T^{0.5} / n_e$ and n_e is the electron number density, following Bakes & Tielens (1994), Wolfire et al. (2003), and Bergin et al. (2004). Here we have assumed that dust shielding is negligible, which is a fair approximation at low metallicity.

We find excellent agreement between GRACKLE and SGCHEM with $\zeta = 10^{-16} \text{ s}^{-1}$ up to $n \lesssim 10^2 \text{ cm}^{-3}$, which is reassuring. In contrast, SGCHEM with $\zeta = 0$ leads to a significantly lower equilibrium temperature for a broad range of densities. This is caused by a severely underestimated electron abundance $x_e \equiv n_e / n$ when CR ionization is switched off, as shown in the upper-right panel of Figure 13 (shown in orange), which in turn strongly underestimates ϵ_{PE} (shown in blue).

The individual cooling and heating processes in SGCHEM are shown in the lower-left (for $\zeta = 10^{-16} \text{ s}^{-1}$) and lower-right (for $\zeta = 0$) panels. For $\zeta = 10^{-16} \text{ s}^{-1}$, heating is dominated by the photoelectric effect at $n > 0.3 \text{ cm}^{-3}$ and by CR ionization at $n < 0.3 \text{ cm}^{-3}$. The total heating rate is almost constant with n , which is balanced by Ly α cooling at low n and by fine-structure line cooling at high n . At $n > 10^3 \text{ cm}^{-3}$, heating from H_2 photodissociation and H_2 formation becomes non-negligible, which might explain the discrepancy in the equilibrium temperature in this regime. In contrast, for $\zeta = 0$, not only does CR ionization heating vanish by construction, but the photoelectric heating is also significantly suppressed, caused by the artificially low electron abundance. As a result, the equilibrium temperature becomes unreasonably low ($T < 10^2 \text{ K}$) even for typical densities in the diffuse ISM. This has been seen in Hu et al. (2017) where

the authors adopted SGCHEM but did not include CR ionization. Interestingly, when applied to the hydrodynamical simulations of Hu et al. (2017), such low temperatures are never reached as SN feedback (and the turbulence it drives) provides extra heating and ionization, which has a similar effect to CR ionization. Therefore, the resulting phase diagram is quite similar to what we found in Figure 4. That said, having a more realistic thermal balance in a static medium is still desirable. We recommend future simulations that use SGCHEM (or other similar chemistry codes) where ϵ_{PE} is calculated via Equation (A1) to always include CR ionization.

To conclude, adopting a constant ϵ_{PE} is a good approximation of the more realistic situation where both the photoelectric effect and CR ionization are present, even though we do not explicitly include the latter. In reality, CR ionization either dominates heating at low densities or provides the crucial free electrons that facilitate photoelectric heating at high densities.

Appendix B Constant Star Formation Timescale

In this section, we present a numerical experiment suggested by the anonymous referee that will further strengthen our conclusion on the importance of SN clustering. As we discussed in Section 3.4, the strong SN clustering in Lagrangian codes is due to the locally enhanced SFR from the superlinear density dependence $\dot{\rho}_* = \epsilon_{\text{SF}} \rho_{\text{gas}} / t_{\text{ff}} \propto \rho_{\text{gas}}^{1.5}$. Here we conduct a simulation using GIZMO with $t_{\text{SN}} = 10 \text{ Myr}$ but with the local SFR $\dot{\rho}_* = \rho_{\text{gas}} / t_{\text{SFR}}$, where $t_{\text{SFR}} = 2 \text{ Gyr}$ is

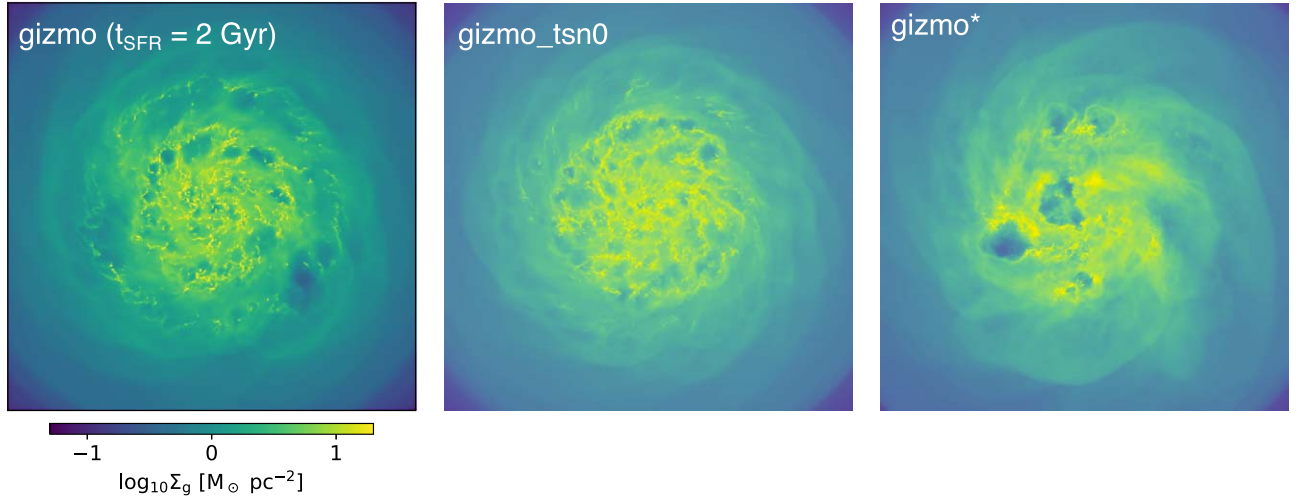


Figure 14. Gas surface density maps of different GIZMO models at $t = 500$ Myr. The constant depletion time model (left) is qualitatively more similar to the *gizmo_tsn0* model with a smooth gas morphology, as opposed to the *gizmo** model, which shows large SN bubbles.

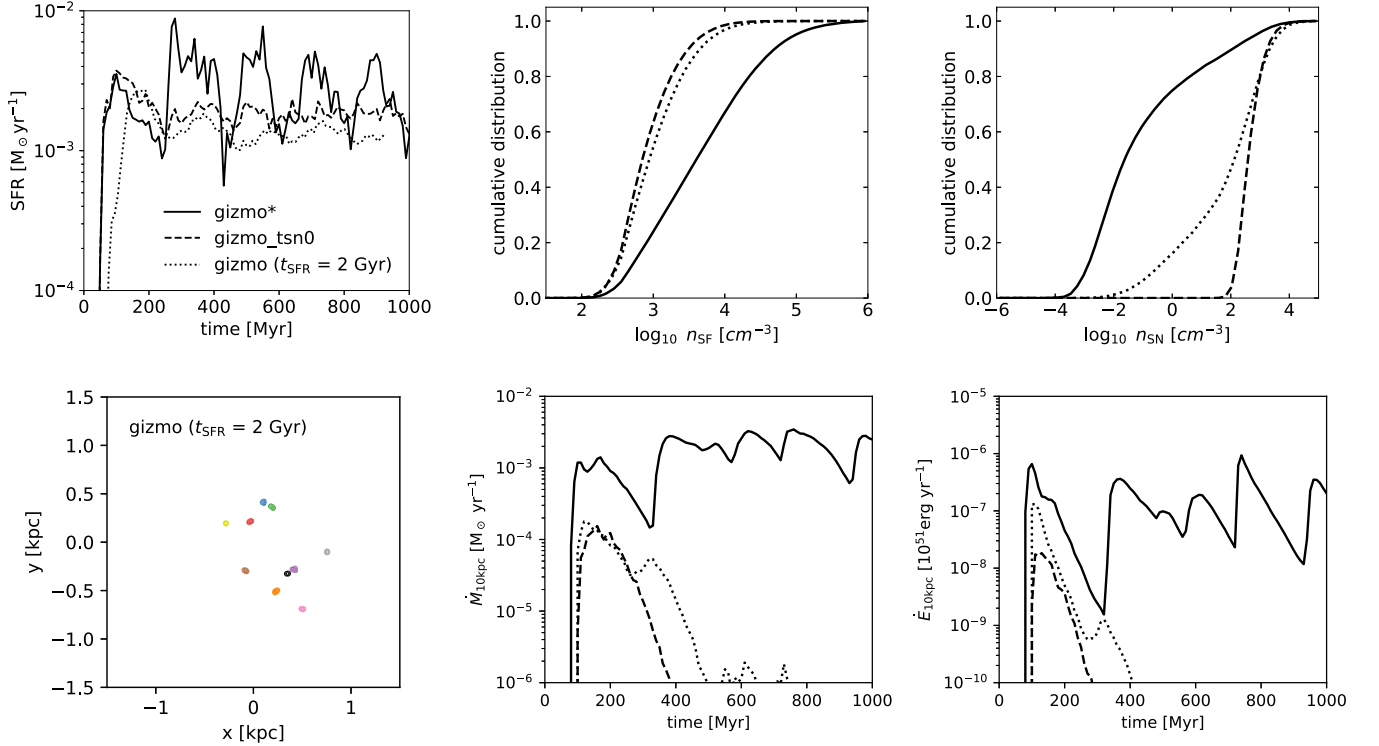


Figure 15. Comparison among *gizmo** (solid), *gizmo_tsn0* (dashed), and the constant depletion time model (dotted). Upper left: SFR as a function of time. Upper middle: cumulative distribution of n_{SF} . Upper right: cumulative distribution of n_{SN} . Lower left: top 10 SN clusters for the constant depletion model only (face-on view). Lower middle: mass outflow rate as a function of time. Lower right: energy outflow rate as a function of time. The constant depletion time model behaves more similarly to the *gizmo_tsn0* model—both have nonbursty star formation and vanishing outflows as a result of low SN clustering.











the local depletion time, which is chosen to be a constant. In other words, the local SFR has a linear (rather than superlinear) dependence on gas density. As shown in Figure 14, this constant depletion time model shows a smooth gas morphology similar to the *gizmo_tsn0* model but with more pronounced dense gas clumps. This is in contrast to the *gizmo** model with large SN bubbles. In addition, as shown in Figure 15, this model shows a smooth, nonbursty SFR as a function of time and cumulative distributions of n_{SF} and n_{SN} similar to those in the *gizmo_tsn0* model. This is because although gas can collapse to densities much higher than the star formation

threshold density, the local SFR is not enhanced, leading to a large number of dense clumps. These clumps, instead of quickly converting into stars as in the *gizmo** model, simply wander around, forming stars at a much lower rate, until they get dispersed by SN feedback after 10 Myr. This leads to low SN clustering, with the maximum $N_{\text{cl}} = 5$ in the entire simulation, which in turn leads to vanishing outflows.

These results support our argument that the superlinear dependence of the local SFR on density $\dot{\rho}_* \propto \rho_{\text{gas}}^{1.5}$ leads to strong SN clustering in Lagrangian codes. Adopting a constant local depletion time can make Lagrangian codes behave more like the

fiducial RAMSES model. However, just like our $t_{\text{SN}} = 0$ models, this is merely a numerical experiment as it implies that the star formation efficiency decreases as density increases, which is not physically justified.

ORCID iDs

Chia-Yu Hu (胡家瑜)  <https://orcid.org/0000-0002-9235-3529>
 Matthew C. Smith  <https://orcid.org/0000-0002-9849-877X>
 Romain Teyssier  <https://orcid.org/0000-0001-7689-0933>
 Greg L. Bryan  <https://orcid.org/0000-0003-2630-9228>
 Andrew Emerick  <https://orcid.org/0000-0003-2807-328X>
 Rachel S. Somerville  <https://orcid.org/0000-0002-6748-6821>
 Blakesley Burkhart  <https://orcid.org/0000-0001-5817-5944>
 Yuan Li (黎原)  <https://orcid.org/0000-0001-5262-6150>
 John C. Forbes  <https://orcid.org/0000-0002-1975-4449>
 Tjitske Starkenburg  <https://orcid.org/0000-0003-2539-8206>

References

- Agertz, O., & Kravtsov, A. V. 2015, *ApJ*, 804, 18
 Agertz, O., Kravtsov, A. V., Leitner, S. N., & Gnedin, N. Y. 2013, *ApJ*, 770, 25
 Agertz, O., Pontzen, A., Read, J. I., et al. 2020, *MNRAS*, 491, 1656
 Bakes, E. L. O., & Tielens, A. G. G. M. 1994, *ApJ*, 427, 822
 Barnes, J., & Hut, P. 1986, *Natur*, 324, 446
 Bate, M. R., & Burkert, A. 1997, *MNRAS*, 288, 1060
 Benincasa, S. M., Wadsley, J., Couchman, H. M. P., & Keller, B. W. 2016, *MNRAS*, 462, 3053
 Bergin, E. A., Hartmann, L. W., Raymond, J. C., & Ballesteros-Paredes, J. 2004, *ApJ*, 612, 921
 Burkhart, B. 2018, *ApJ*, 863, 118
 Burkhart, B., & Mocz, P. 2019, *ApJ*, 879, 129
 Calura, F., Lupi, A., Rosdahl, J., et al. 2022, *MNRAS*, 516, 5914
 Cullen, L., & Dehnen, W. 2010, *MNRAS*, 408, 669
 de Mink, S. E., Sana, H., Langer, N., Izzard, R. G., & Schneider, F. R. N. 2014, *ApJ*, 782, 7
 Dehnen, W., & Aly, H. 2012, *MNRAS*, 425, 1068
 Durrer, F., & Dalla Vecchia, C. 2012, *MNRAS*, 419, 465
 Emerick, A., Bryan, G. L., & Mac Low, M.-M. 2019, *MNRAS*, 482, 1304
 Federrath, C., & Klessen, R. S. 2012, *ApJ*, 761, 156
 Forbes, J. C., Krumholz, M. R., Goldbaum, N. J., & Dekel, A. 2016, *Natur*, 535, 523
 Gaburov, E., & Nitadori, K. 2011, *MNRAS*, 414, 129
 Gatto, A., Walch, S., Low, M.-M. M., et al. 2015, *MNRAS*, 449, 1057
 Gatto, A., Walch, S., Naab, T., et al. 2017, *MNRAS*, 466, 1903
 Gentry, E. S., Krumholz, M. R., Dekel, A., & Madau, P. 2017, *MNRAS*, 465, 2471
 Girichidis, P., Walch, S., Naab, T., et al. 2016, *MNRAS*, 456, 3432
 Glover, S. C. O., & Clark, P. C. 2012, *MNRAS*, 421, 116
 Glover, S. C. O., & Mac Low, M.-M. 2007, *ApJS*, 169, 239
 Guillet, T., & Teyssier, R. 2011, *JCoPh*, 230, 4756
 Gutcke, T. A., Pakmor, R., Naab, T., & Springel, V. 2021, *MNRAS*, 501, 5597
 Gutcke, T. A., Pakmor, R., Naab, T., & Springel, V. 2022, *MNRAS*, 513, 1372
 Habing, H. J. 1968, *BAN*, 19, 421
 Hennebelle, P., & Chabrier, G. 2008, *ApJ*, 684, 395
 Hislop, J. M., Naab, T., Steinwandel, U. P., et al. 2022, *MNRAS*, 509, 5938
 Hopkins, P. F. 2015, *MNRAS*, 450, 53
 Hopkins, P. F., Kereš, D., Oñorbe, J., et al. 2014, *MNRAS*, 445, 581
 Hopkins, P. F., Wetzel, A., Kereš, D., et al. 2018, *MNRAS*, 480, 800
 Hu, C.-Y. 2019, *MNRAS*, 483, 3363
 Hu, C.-Y., Naab, T., Glover, S. C. O., Walch, S., & Clark, P. C. 2017, *MNRAS*, 471, 2151
 Hu, C.-Y., Naab, T., Walch, S., Glover, S. C. O., & Clark, P. C. 2016, *MNRAS*, 458, 3528
 Hu, C.-Y., Naab, T., Walch, S., Moster, B. P., & Oser, L. 2014, *MNRAS*, 443, 1173
 Hu, C.-Y., Sternberg, A., & van Dishoeck, E. F. 2021, *ApJ*, 920, 44
 Hunter, D. A., Elmegreen, B. G., & Ludka, B. C. 2010, *AJ*, 139, 447
 Ibáñez-Mejía, J. C., Mac Low, M.-M., Klessen, R. S., & Baczynski, C. 2016, *ApJ*, 824, 41
 Indriolo, N., & McCall, B. J. 2012, *ApJ*, 745, 91
 Keller, B. W., & Kruijssen, J. M. D. 2022, *MNRAS*, 512, 199
 Kim, C.-G., & Ostriker, E. C. 2015, *ApJ*, 802, 99
 Kim, C.-G., & Ostriker, E. C. 2017, *ApJ*, 846, 133
 Kim, C.-G., & Ostriker, E. C. 2018, *ApJ*, 853, 173
 Kim, C.-G., Ostriker, E. C., & Raileanu, R. 2017, *ApJ*, 834, 25
 Kim, C.-G., Ostriker, E. C., Somerville, R. S., et al. 2020, *ApJ*, 900, 61
 Kim, J.-h., Agertz, O., Teyssier, R., et al. 2016, *ApJ*, 833, 202
 Kimm, T., Cen, R., Devriendt, J., Dubois, Y., & Slyz, A. 2015, *MNRAS*, 451, 2900
 Kretschmer, M., & Teyssier, R. 2020, *MNRAS*, 492, 1385
 Krumholz, M. R., & McKee, C. F. 2005, *ApJ*, 630, 250
 Lahén, N., Naab, T., Johansson, P. H., et al. 2019, *ApJL*, 879, L18
 Lahén, N., Naab, T., Johansson, P. H., et al. 2020, *ApJ*, 891, 2
 Leaman, R., Venn, K. A., Brooks, A. M., et al. 2012, *ApJ*, 750, 33
 Li, M., Bryan, G. L., & Ostriker, J. P. 2017, *ApJ*, 841, 101
 Lucy, L. B. 1977, *AJ*, 82, 1013
 Marinacci, F., Sales, L. V., Vogelsberger, M., Torrey, P., & Springel, V. 2019, *MNRAS*, 489, 4233
 Martizzi, D., Fielding, D., Faucher-Giguère, C.-A., & Quataert, E. 2016, *MNRAS*, 459, 2311
 McQuinn, K. B. W., van Zee, L., & Skillman, E. D. 2019, *ApJ*, 886, 74
 Mondal, C., Subramaniam, A., & George, K. 2018, *AJ*, 156, 109
 Naab, T., & Ostriker, J. P. 2017, *ARA&A*, 55, 59
 Navarro, J. F., Frenk, C. S., & White, S. D. M. 1997, *ApJ*, 490, 493
 Orr, M. E., Fielding, D. B., Hayward, C. C., & Burkhart, B. 2022, *ApJ*, 932, 88
 Padoan, P., & Nordlund, Å. 2011, *ApJ*, 730, 40
 Pakmor, R., Springel, V., Bauer, A., et al. 2016, *MNRAS*, 455, 1134
 Price, D. J. 2008, *JCoPh*, 227, 10040
 Rantala, A., Naab, T., & Springel, V. 2021, *MNRAS*, 502, 5546
 Rathjen, T.-E., Naab, T., Girichidis, P., et al. 2021, *MNRAS*, 504, 1039
 Rémy-Ruyer, A., Madden, S. C., Galliano, F., et al. 2014, *A&A*, 563, A31
 Rubio, M., Elmegreen, B. G., Hunter, D. A., et al. 2015, *Natur*, 525, 218
 Scannapieco, C., Wadepuhl, M., Parry, O. H., et al. 2012, *MNRAS*, 423, 1726
 Semenov, V. A., Kravtsov, A. V., & Gnedin, N. Y. 2016, *ApJ*, 826, 200
 Semenov, V. A., Kravtsov, A. V., & Gnedin, N. Y. 2017, *ApJ*, 845, 133
 Simpson, C. M., Bryan, G. L., Hummels, C., & Ostriker, J. P. 2015, *ApJ*, 809, 69
 Smith, B. D., Bryan, G. L., Glover, S. C. O., et al. 2017, *MNRAS*, 466, 2217
 Smith, M. C. 2021, *MNRAS*, 502, 5417
 Smith, M. C., Bryan, G. L., Somerville, R. S., et al. 2021, *MNRAS*, 506, 3882
 Smith, M. C., Sijacki, D., & Shen, S. 2018, *MNRAS*, 478, 302
 Smith, R. J., Treß, R. G., Sormani, M. C., et al. 2020, *MNRAS*, 492, 1594
 Somerville, R. S., & Davé, R. 2015, *ARA&A*, 53, 51
 Springel, V. 2005, *MNRAS*, 364, 1105
 Springel, V. 2010, *MNRAS*, 401, 791
 Springel, V., Di Matteo, T., & Hernquist, L. 2005, *MNRAS*, 361, 776
 Steinwandel, U. P., Bryan, G. L., Somerville, R. S., Hayward, C. C., & Burkhart, B. 2022, arXiv:2205.09774
 Steinwandel, U. P., Moster, B. P., Naab, T., Hu, C.-Y., & Walch, S. 2020, *MNRAS*, 495, 1035
 Teyssier, R. 2002, *A&A*, 385, 337
 Truelove, J. K., Klein, R. I., McKee, C. F., et al. 1997, *ApJL*, 489, L179
 Walch, S., Girichidis, P., Naab, T., et al. 2015, *MNRAS*, 454, 238
 Wall, J. E., Mac Low, M.-M., McMillan, S. L. W., et al. 2020, *ApJ*, 904, 192
 Weinberger, R., Springel, V., & Pakmor, R. 2020, *ApJS*, 248, 32
 Wheeler, C., Hopkins, P. F., Pace, A. B., et al. 2019, *MNRAS*, 490, 4447
 Wolfire, M. G., McKee, C. F., Hollenbach, D., & Tielens, A. G. G. M. 2003, *ApJ*, 587, 278